Structural & Magnetic Investigations of Corundum & Perovskite Structures of the Compound AMO_3

A thesis submitted in partial fulfilment
for the degree of

Master of Science

as a part of the

Integrated Ph.D. programme
(Materials Science)

by

Pavitra Nityanand Shanbhag

Chemistry and Physics of Materials Unit
Jawaharlal Nehru Centre for Advanced
Scientific Research
(A Deemed University)
Bangalore, India

March 2017

Dedicated to my parents

DECLARATION

I hereby declare that the matter embodied in this M.S. thesis entitled **"Structural & Magnetic Investigations of Corundum & Perovskite Structures of the Compound AMO_3"** is the outcome of investigations carried out by me under the supervision of Prof. A. Sundaresan at the Chemistry and Physics of Materials Unit, Jawaharlal Nehru Centre for Advanced Scientific Research, Bangalore, India and this work is unique being submitted nowhere else for the award of any degree or diploma.

Thus going with the pre-existing practice of reporting scientific observations, due acknowledgement has been made whenever a work represented mentioned is based on the findings of other investigators.

31/03/2017

Pavitra Nityanand Shanbhag

CERTIFICATE

I hereby certify that the matter embodied in this M.S. thesis entitled **"Structural & Magnetic Investigations of Corundum & Perovskite Structures of the Compound AMO_3"** has been carried out by Ms. Pavitra Nityanand Shanbhag at the Chemistry and Physics of Materials Unit, Jawaharlal Nehru Centre for Advanced Scientific Research, Bangalore, India under my supervision and it has not been submitted elsewhere for the award of any degree or diploma.

31/03/2017

Prof. A. Sundaresan

(Research Supervisor)

Acknowledgements

I am extremely grateful to my supervisor *Prof. A. Sundaresan* for being helpful to me all the time with generous guidance and constant encouragement. So I take this opportunity to express my immense gratitude to him. I sincerely thank him for providing interesting research problems and freedom to perform all my experiments. It has been a great pleasure for me to work under his guidance.

Prof. C. N. R. Rao, FRS has been a great source of inspiration during my MS work. I would like to sincerely thank him for having useful scientific discussions and providing us all the experimental facilities.

I convey my sincere thanks to past and present CPMU chairmen, *Prof. Balasubramanian* and *Prof. Chandrabhas Narayana* for providing all the experimental facilities.

I thank the past and present Int. Ph. D. conveners, *Prof. Chandrabhas Narayana* and *Prof. M. Eswaramoorthy*.

My heartfelt thanks to all my present lab mates, *Mr. Somnath, Mr. Chandan, Mr. Abhijit, Mr. Amit, Mr. Ravishankar, Mr. Premkumar, Mr. Chandraih* and past labmates *Dr. Rambabu, Dr. Rana* for giving me a friendly atmosphere in lab, guiding me for my research problem, helping me through the whole period to learn various measurement techniques and their constant support for my work.

I would like to express my sincere gratitude to all the faculty members of the Chemistry and Physics of Materials Unit and *Prof. T.N. Guru Row* of Solid State and Structural Chemistry Unit, IISC for offering their fruitful courses.

I would like to thank technical staffs *Mr.Anil, Mrs. Selvi, Mr. Ala Sreenivas, Mr. Sunil, Mr. srinath, Mr. Vasu* for their help in various techniques and difficulties.

I would like to acknowledge *Prof. Shiv Halasyamani, University of Houston, USA* for SHG measurements.

I would like to thank my batchmates *Srimayee, Anaranya, Anirudha, shikha* and *Ekashmi* for their cheerful company and extended help throughout the period.

I would also like to thank my past school and college teachers for making me understand basic concepts of science.

I would like to thank *Mr. Muralidhar Prabhu* and *Mr. Vasanth Bhat* for their help and support.

I would like to specially thank *Mr. Bharath* and other friends *Mr. Nagaraj, Mr. Murali, Mr. Sridhara, Mrs. Kiruthika, Mr. Shobhin, Mr.Shivram, Ms. Divya, Ms. Priyanka and* seniors *Mr. Priyank, Ms. Nikita, Mr. abhiroop, Ms. Sunita* who have been supportive in all situation.

Above all, I would like to thank my parents, sister, brother and my cousins for all the love, affection and support to my research work.

Preface

In this thesis we report our investigations on corundum type transition metal oxides and their interesting magnetic properties. Most of the compounds are stabilised in corundum structure by high pressure synthesis. Also, cobalt oxides forming solid solutions with rare earth oxides exhibiting intermediate spin state are studied. Most of the oxides in the present work have cation site disorder which gives rise to spin glass state at low temperature.

Chapter 1 deals with introductory concepts of transition metal oxides. Crystal structure diversity, interesting properties and phenomena of transition metal oxides has been discussed.

Chapter 2 narrates different types of synthesis, their basic principles and characterization methods carried out during the course of research.

Chapter 3 describes the high pressure synthesis and magnetic properties of corundum type $Ga_{1-x}Al_xFeO_3$ (x=0, 0.5) family of oxides and decomposition of orthorhombic $AlFeO_3$ under high pressure and high temperature.

Chapter 4 explains synthesis and comparative magnetic study of $ACrO_3$ (A=Al, Ga) compounds and effect of Fe substitution in $AlCrO_3$ on its magnetic properties.

Chapter 5 explains existence of elusive Co_2O_3 in the form of solid solution with Y_2O_3 and Lu_2O_3 where cobalt exhibits unusual intermediate spin state and study of their magnetic properties under high pressure.

Contents

Chapter 1

Introduction

1.1. Transition Metal Oxides

Transition metal oxides occur with a huge diversity of crystal structures, which is manifested in the abundance of their physical and chemical properties. The structure-property relationship in these transition metal oxides is greatly influenced by the orbital states of their electrons and their correlations [1]. Transition metal oxides show a variety of phenomena, which are technologically important and have found many applications in industry. Most of the interesting phenomena in condensed matter physics such as ferromagnetism, antiferromagnetism, ferrimagnetism, colossal magnetoresistance, ferroelectricity, antiferroelectricity, piezoelectricity, high T_c superconductivity, Mott transition, spin state transition multiferroicity, spin glass state, spin ice state and quantum spin liquid state are exhibited by transition metal oxides. All these emergent phenomena observed in the transition metal oxides are owing to the presence of d electrons and oxygen ions surrounding it. These d-electrons have their own internal degrees freedom namely charge, spin and orbital. These degrees of freedom collectively lead to all the fascinating properties listed above. During the formation of transition metal oxides, oxygen ions surrounds the transition metal in different geometry and hence transition metal experience static electric field which is known as crystal field produced by the surrounding oxygen anions. This results in splitting of degenerate d-orbitals into non degenerate orbitals depending on the symmetry of the approaching oxygen ions. In case of octahedral symmetry, five d orbitals split into three t_{2g} orbitals (d_{xy}, d_{xz}, d_{yz}) and two e_g orbitals ($d_{x^2-y^2}$, d_{z^2}), which is very common in materials with three dimensional perovskite (ABO_3) crystal structure. Also, unpaired d-electrons

with their spin show two different features i.e. itinerant (freely roaming) and localized (tightly bound) give rise to incredible phenomena beyond the researcher's vision. Electrical properties of transition metal oxides range from superconducting to insulating behavior. According to band theory, presence of unpaired electrons is the cause of electrical conductivity of the material but monoxides of Fe^{2+}, Mn^{2+} and Co^{2+} are insulators even though they have unpaired electrons. To understand the electronic properties of such insulators Mott-Hubbard model has been introduced. According to this model, the electrostatic repulsions between the electrons results in their localization on one site and splitting of d-band to give large energy gap, makes them insulating. Also, much celebrated high T_c superconductors of cuprate family of oxides have begun a new era in condensed matter physics with new concepts like resonating valence bond theory by P.W. Anderson which later has been used to explain new quantum state of matter so called quantum spin liquid. In the following, structural variety of transition metal oxides, phenomena and properties has been discussed.

1.1.1. Structural Diversity:

Considering the oxidation states for transition metals, in case of 3d series, it ranges from +1 to +7 whereas 4d series can have from +1 to +8 and 5d series from +2 to +9. Hence, existence of such great variety of oxidation states in transition metals result in the formation of transition metal oxides in different forms such as MO, MO_2, M_2O, MO_3, M_2O_3, M_3O_4 and M_2O_5. Other than M_3O_4 in all other forms transition metals exist in single oxidation state where in case of M_3O_4 transition metal exist in both M^{2+} and M^{3+} state. Transition metal monoxides, MO mainly adopts rock salt type structure but some of them have wurtzite and platinum sulphide type structure whereas dioxides, MO_2 mostly exist in rutile structure but some crystallize in fluorite

structure. Dioxides exhibit diversity in their crystal structure known as polymorphism. For example, TiO_2 can have three different crystal structures namely rutile, anatase and brookite. Very few binary oxides such as Ag_2O and Cu_2O exist in M_2O stoichiometric form and adopt cuprite structure. Further, transition metal sesquioxides, M_2O_3 mostly attain corundum structure in which oxygen anions forms hexagonal close packed array and M^{3+} cations occupy two thirds of the octahedral holes. Spinels, ($M^{2+}[M^{3+}]O_4$) are the unique class of oxides which show two different oxidation states for transition metal and very few transition metals namely Fe, Mn, Co exhibit this structure. Also, pentoxides, M_2O_5 are the group of oxides formed by limited transition metals such as V, Nb and Ta. Trioxides, MO_3 are another stoichiometric form attained by oxides of elements Cr, W, Mo and Re where ReO_3 attains famous perovskite structure. In addition to all these stoichiometric forms, transition metal oxides also exist in M_2O_7, MO_4 and many complex structures. Transition metals in two different oxidation states also exist in some uncommon oxides like, Cr_5O_{12}, V_6O_{13} and Mn_5O_8. Combination of any elemental oxide with binary transition metal oxide results in huge variety of crystal structures and also leads to fascinating and interesting properties to the resulting ternary oxides. Generally, ternary transition metal oxides adopts spinel structure (AB_2O_4), perovskite structure (ABO_3), pyrochlore Structure ($A_2B_2O_7$), Ruddlesden-Popper series ($A_{n-1}A'_2B_nX_{3n+1}$), garnets ($A_3B'_2B''_3O_{12}$) and delafossite structure (ABO_2) and many different complex structures.

Spinels: Spinels are a class of materials with general formula AB_2X_4 where A is bivalent cation, B is trivalent cation and X is divalent anion and it named so because of mineral $MgAl_2O_4$. Oxygen anions adopt cubic close packed structure in spinel. Depending on the occupancy of A and B cations in tetrahedral and octahedral sites, spinels can be classified as normal and inverse. In case of normal spinel, tetrahedral voids are occupied by divalent A cations and octahedral

voids are occupied by trivalent B cations. Mn_3O_4, $ZnFe_2O_4$, $MgAl_2O_4$, $FeCr_2O_4$, Co_3O_4 etc. belong to class of normal spinels. Whereas in inverse spinels, the divalent A cations occupy octahedral voids and half of the trivalent cations occupy tetrahedral voids. Another half of trivalent cations occupy octahedral voids. Fe_3O_4, $CoFe_2O_4$ and $NiFe_2O_4$ etc. belong to the group of inverse spinels.

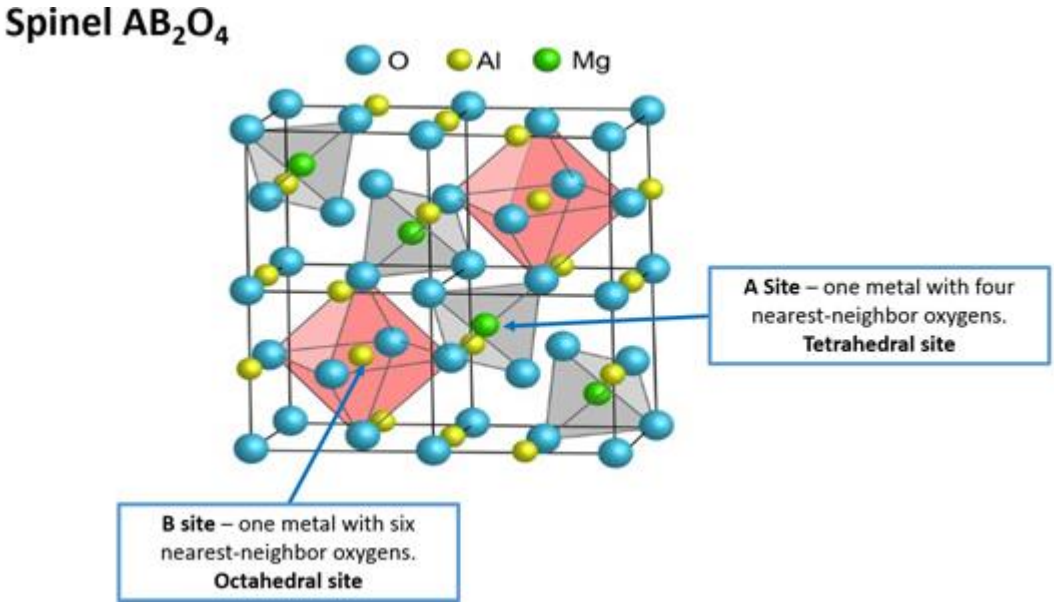

Fig. 1.1. Typical spinel structure [47]**:**

Perovskites: Most of the materials with general form ABO_3 adopt perovskite structure. The crystal structure of mineral $CaTiO_3$ is named as Perovskite structure in the honor of Russian mineralogist Lev Perovski. Perovskites consist of cations A and B which can be of different size, oxidation state and has corner sharing BO_6 octahedra. It consists of eight BO_6 octahedra which creates hole at the centre and is occupied by the cation A. Hence, A cation attains 12-fold oxygen coordination and B cation attains 6 fold oxygen coordination. The ideal perovskite structure is found for tolerance factor t=1 ($t = \frac{(r_A+r_o)}{[\sqrt{2}(r_B+r_o)]}$, where r_A, r_B and r_o are radii of A cation, B cation and anion respectively [7]). For t < 1, it undergoes various structural transition and exhibits very

interesting properties such as ferroelectricity ($BaTiO_3$), piezoelectricity ($Pb(Zr_xTi_{1-x})O_3$), superconductivity ($BaBiO_3$) gaint nagneto resistance ($LaMnO_3$,$LaNiO_3$) and has found application in solar cell devices.

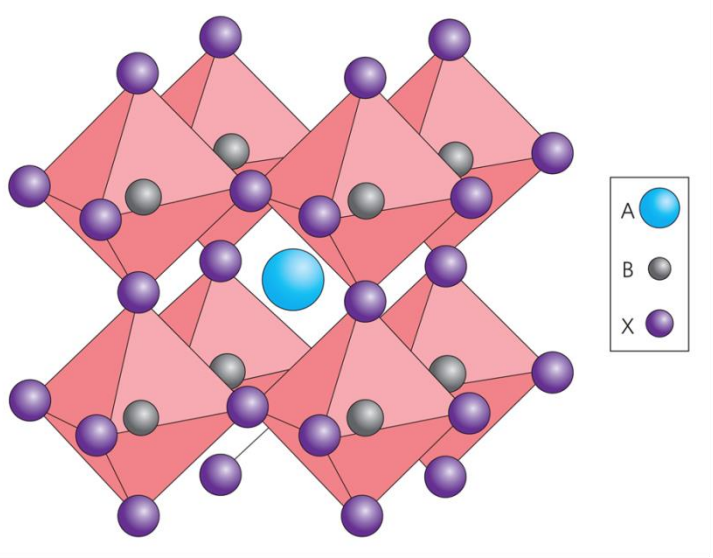

Fig. 1.2. Typical Perovskite structure [48]

Garnets: Garnets are group of oxides with mixed framework with the stoichiometric form $A_3B'_2B''_3O_{12}$. Crystal structure consists of corner sharing $B''O_6$ octahedra and $B'O_4$ tetrahedra constituting three dimensional lattice, $B'_2B''_3O_{12}$. Each tetrahedron is connected to four octahedra whereas each octahedron is connected to six tetrahedra. Hence, octahedron $B''O_6$ alternates tetrahedron $B'O_4$ to form a row along <110> direction, (c.f. figure 1.8) [4]. Materials such as, $Ln_xFe_5O_{12}$ (x = 3 for Tb, Gd, Nd, Sm, Eu, Ho so on. and 2 for Dy) [4], crystallize in this structure. Nonlinear optical properties are the main focus of interest in this class of materials. Gadolinium Gallium Garnet, $Gd_3Ga_2(GaO_4)_3$ is a synthetic garnet specially used as a substrate for liquid phase epitaxy of magnetic garnet films.

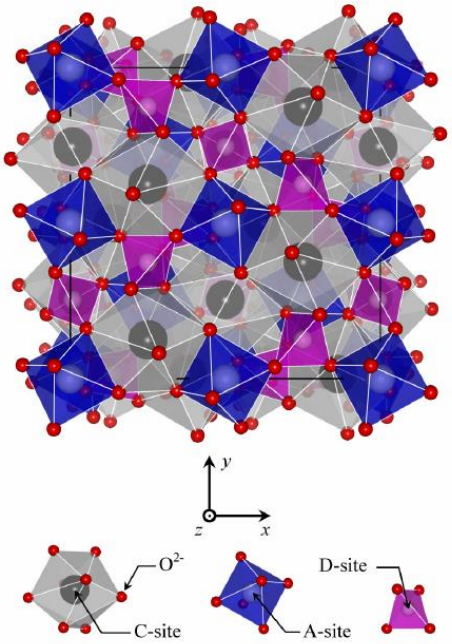

Fig.1.3.Unit cell of garnet-type structure $C_3A_2D_3O_{12}$ [49]

Pyrochlores: This class of materials mostly exists in $A_2B_2O_7$ stoichiometric form where A can be rare earth ion & B is transition metal and attains cubic crystal structure (Fd-3m). In pyrochlores, each unit cell consists of 8 formula units. Pyrochlore structure is a derived form of fluorite structure AX_2 but the only difference is the absence of one eighth of the anions and there are two different cation sites in pyrochlores, as shown in the fig.4. [2]. This group of materials exhibit variety of properties such as superconductors ($Cd_2Re_2O_7$), spin glass systems ($Y_2Mo_2O_7$), ionic conductors ($Gd_{1.9}Ca_{0.1}Ti_2O_{6.9}$), electronic insulators ($La_2Zr_2O_7$), metallic conductors ($Bi_2Ru_2O_{7-y}$), spin ice systems ($Dy_2Ti_2O_7$) and haldane chain systems ($Tl_2Ru_2O_7$) and so on.

Delafossites: Most of the materials with general form ABO_2, where A is monovalent and B is trivalent ions, adopt delafossite structure. It has a crystal structure of mineral $CuFeO_2$. The crystal structure consist of stacked sheets of linearly coordinated A cations between edge shared

octahedral BO_6 layers [3]. This class of material is famous for their electrical properties from metallic to insulating [3]. The crystal structure has two planar layers alternating each other where one layer has triangularly arranged A cations and another layer is of edge sharing BO_6 octahedra compacted along c-axis. $CuAlO_2$ is a famous transparent conducting oxide belonging to this family of oxides.

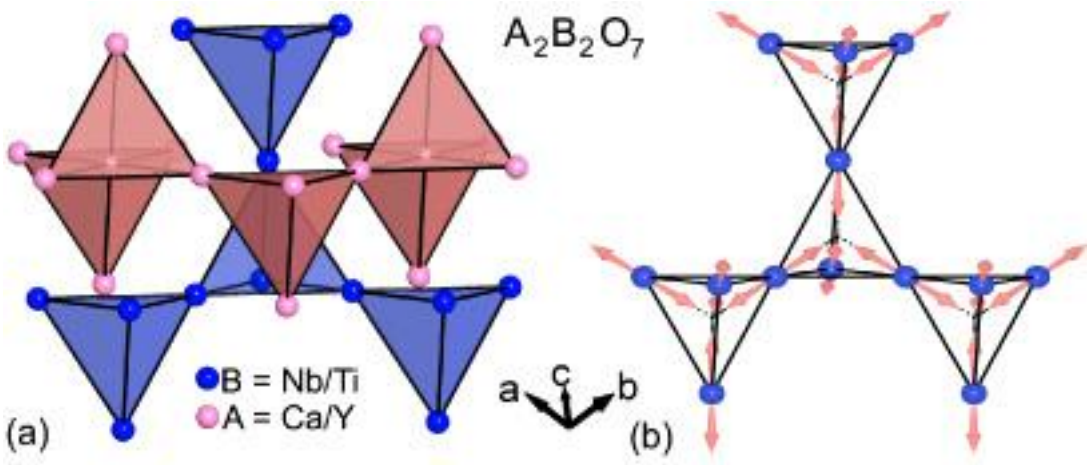

Fig.1.4. Typical pyrochlore $A_2B_2O_7$ crystal structure [50]

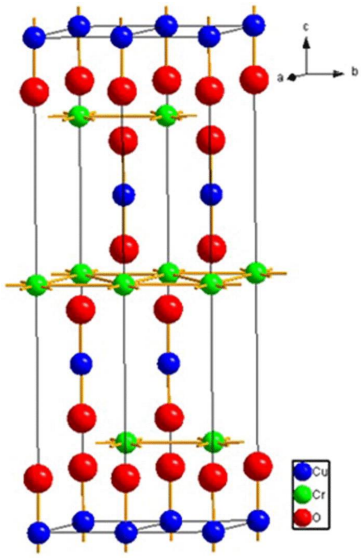

Fig.1.5. Typical delafossite crystal structure [51]

Ruddlesden-Popper series: Materials of this class are having general formula $A_{n-1}A'_2B_nX_{3n+1}$ where A, A', B are cations and X is anion. Here n is number of layers consisting of octahedra in perovskite like stack. Crystal structure consists of 2 D perovskite blocks interconnected with cations. Here, B is transition metal where A, A' can be rare earth, alkali or alkaline earth metal. A cations are situated in perovskite layers and have 12- fold (cuboctahedral) anionic coordination whereas A' cations are situated at the perovskite boundary with a separating block layer and B cations are situated at the centre of the anionic squares, octahedral or pyramids[5]. $LaSr_3FeO_{10}$ is one of the Ruddlesden-Popper phases, which have found application in rechargeable metal air battery [6].

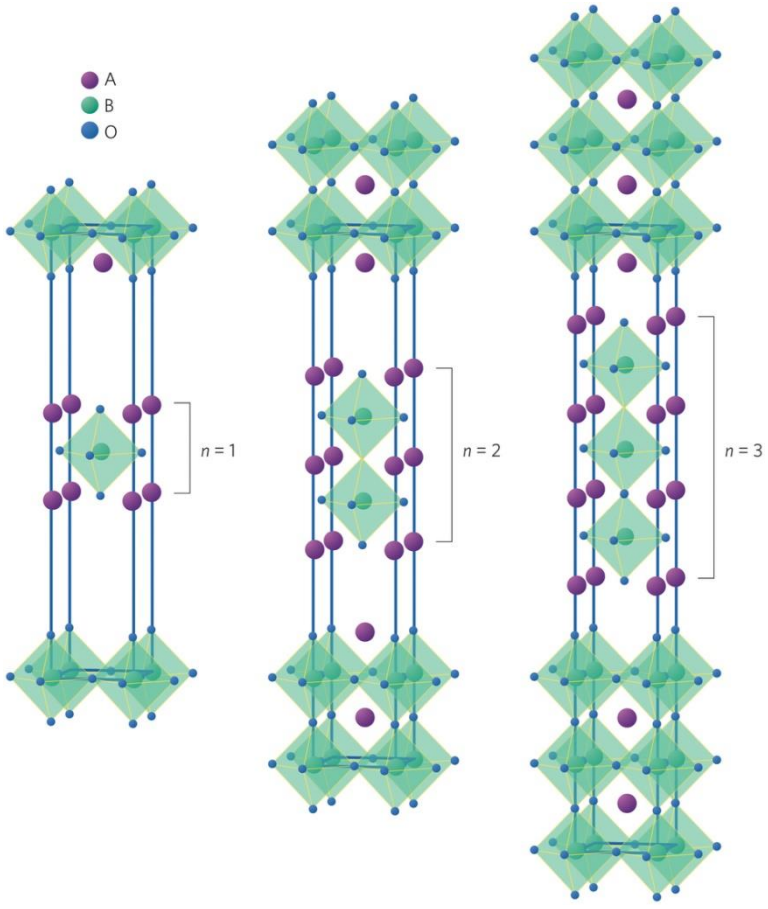

Fig.1.6. Ruddlesden-Popper series $A_{n+1}B_nX_{3n+1}$ crystal structure [52]

1.1.2. Diverse Phenomena and Properties:

Transition metal oxides exhibit a wide variety of phenomena and diverse properties, which are worth studying. External perturbations like electric field, magnetic field, temperature, and mechanical stress etc. act as external forces and lead to changes in the properties of these oxides. Some of the important phenomena like John Teller effect, exchange interactions, frustrated magnetism, magnetoelectric coupling has been discussed below.

1.1.2.1. Electronic Properties:

I. Jahn Teller Effect:

Jahn-Teller effect is a phenomenon that describes distortion of the geometry of transition metal ions associated with definite electronic configuration. Jahn-Teller theorem states, "any non-linear molecule with degenerate electronic state is unstable and undergoes distortion to lower symmetry resulting in minimization of energy thereby removing the degeneracy" [13]. The JT distortion is observed for low-spin Ni^{3+} (d^7) and high spin Cu^{2+}(d^9), Mn^{3+}(d^4) ions. $LaMnO_3$ is one of the transition metal oxides showing Jahn-Teller distortion. In case of $LaMnO_3$, Mn^{3+} is having degenerate electronic states and hence it can be called as Jahn-Teller ion. In the unit cell of $LaMnO_3$, it is located at the octahedral hole created by surrounding oxygen ions. Because of the oxygen anion crystal field, the five d orbitals split into three t_{2g} orbitals with lower in energy and two e_g orbitals with higher energy. Further splitting of e_g orbitals takes place to break the degeneracy and the octahedron become distorted. There are different kinds of Jahn Teller effect such as static where the distorted octahedrons fixed along certain axis and another type is cooperative where distorted octahedrons interact cooperatively and undergo structural phase

transitions. Spinels such as $FeCr_2O_4$ and FeV_2O_4 [14] have found to show this cooperative Jahn-Teller effect.

II. Spin state degrees of freedom:

3d transition metal ions mostly exhibit either high spin state or low spin state but some transition metal ions such as Co in $LaCoO_3$ [61] and Fe in porphyrinato iron(III) complexes[62] found to exhibit intermediate spin state. The theory behind such unusual spin state is complicated. In case of Co^{3+} three spin states are possible. i.e. high spin state ($t_{2g}^4 e_g^2,\ S = 2$), low spin sate ($t_{2g}^6 e_g^0,\ S = 0$) and intermediate spin state ($t_{2g}^5 e_g^1,\ S = 1$). If the crystal field splitting energy (E_{Cf}) is smaller than that of pairing energy (E_P) then Co^{3+} attains high spin otherwise Co^{3+} attains high spin state but when E_p and E_{cf} is of same order Co^{3+} attains intermediate spin state [63].

1.1.2.2. Magnetic Properties:

In correlated systems, the overlapping of atomic orbitals of neighboring atoms give rise to interatomic exchange interaction. To minimize the energy of the crystal and in accordance with Pauli's Exclusion principle, orientation of the spins lead to the origin of particular type of magnetism. These interactions are quantum mechanical in nature. Generally, the exchange energy can be given by the Eigen value of the Heisenberg spin Hamiltonian operator,

$$\hat{H} = -\sum_{i<j} J_{ij}\, \hat{S}_i \cdot \hat{S}_j$$

Where, J_{ij} is the exchange integral describing the coupling between two i_{th} and j_{th} spins.

For $J_{ij} > 1$, spins align parallel giving rise to ferromagnetism and for $J_{ij} < 1$, spins align antiparallel giving rise to antiferromagnetism to minimize the energy. Here three different

interactions come into picture. i.e. 1) Direct exchange, 2) Indirect Exchange and 3) Superexchange.

I. Direct Exchange:

Direct exchange works between magnetic ions, which are close to each other so that to have maximum overlap of their wave functions. It operates without any involvement of mediator. This type of interaction is very strong but limits to short distance and hence the effect decreases as the magnetic ions get separated. Since the interaction is short ranged, according to Pauli's Exclusion principle the spins can align antiparallel, which results in antiferromagnetic coupling between the neighboring magnetic ions.

II. Indirect Exchange:

Indirect exchange interaction operates over large distances. Here, the exchange between the magnetic ions takes place through a mediator, which can be electrons in case of metals, and hence it is called indirect exchange. This interaction is called as RKKY (Ruderman, Kittel, Kasuya and Yoshida) interaction. In metals, spin polarization will be induced by localized moment in its neighboring itinerant electrons which in turn polarize the neighboring magnetic moment and hence establish long range magnetic ordering and follows oscillatory behavior. So, depending on the distance between magnetic ions, the interaction will lead to either ferromagnetic or antiferromagnetic behavior of material [8-10].

III. Superexchange:

This is another type of indirect exchange where the non-neighboring magnetic moments coupled by nonmagnetic ion situated between magnetic ions. In the case of transition metal oxide, MnO, the intermediate oxygen anion O^{2-} virtually transfers electron in the 2p orbital to the neighboring magnetic ion Mn^{2+}. Due to the covalent mixing of d orbital of Mn^{2+} ion and p

orbital of O^{2-} ion, the spin of the 3d electron favors antiparallel alignment with the spin of 2p electron. Another electron in the same orbital (2p) of oxygen is antiparallel with the first 2p electron according to Pauli's Exclusion principle. Hence, on the other side Mn^{2+} ion has spin that is antiparallel to first Mn^{2+} ion. This way the superexchange leads to antiparallel alignment of spins if the cation-anion-cation bond angle is 180^{o}. If the cation-anion-cation bond angle is 90^{o}, then interaction leads to ferromagnetic ordering. This exchange interaction occurs between the magnetic ions of same valence.

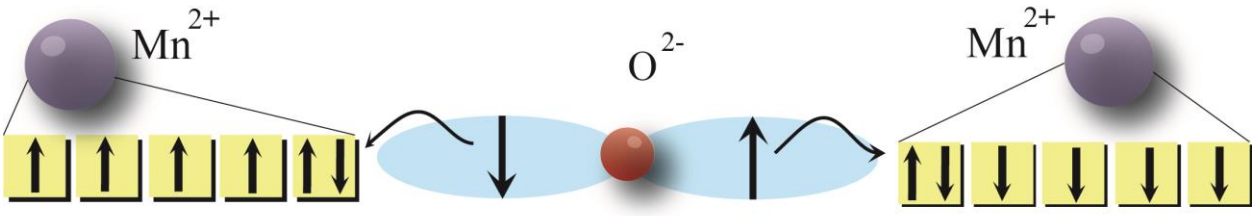

Fig.1.7. Super exchange interaction in MnO [53]

IV. Double Exchange:

This kind of exchange interaction occurs between the magnetic ions of different oxidation states. The strontium doped lanthanum manganates $La_{1-x}Sr_xMnO_3$ ($0 \leq x \leq 1$) consist of x fraction of the Mn^{4+} ions and (1-x) fraction of Mn^{3+} ions [11]. Mn^{4+} ions have empty e_g orbitals whereas Mn^{3+} ions have one electron in its e_g orbital. Hence, electron from Mn^{3+} e_g orbital hops to Mn^{4+} via oxygen ion, O^{2-}. According to Hund's rule, after the transfer of electron the spin will get preserved if both manganese ions have same spin alignment. Hence, double exchange interaction is energetically more favorable for the magnetic ions having same spin alignment than being opposite as shown in figure 6. This way, double exchange interaction favors ferromagnetic ordering and hopping of electrons through the crystal makes the material metallic.

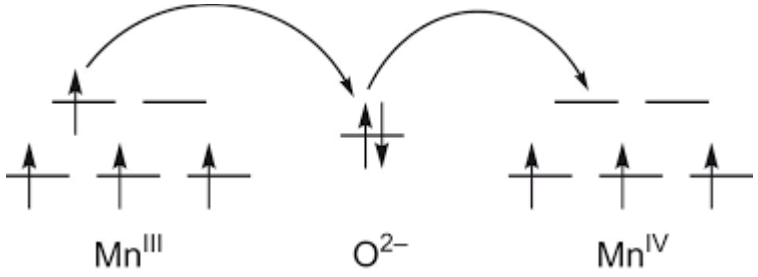

Fig.1.8. Double exchange interaction Mn^{3+} and Mn^{4+} ions [54]

V. Frustrated magnetism:

The competition between exchange interactions in the crystal lattice can lead to new magnetic ground states like spin glass, spin ice and quantum spin liquid states. All these are magnetically disordered near absolute zero temperature. Here, only spin glass state observed in transition metal oxides has been explained briefly.

Spin Glass: It's a type of magnetic response exhibited by many transition metal oxides near absolute zero temperature. In these systems, crystalline lattices have a kind of frustration caused by competitive ferromagnetic and antiferromagnetic interactions, which makes the system magnetically disordered at lower temperatures. Here, the spins of the magnetic ions get freeze in random orientations and hence the resulting disorder is called quenched disorder. Also the disorder observed in the lattice is not structural but magnetic. Because of spin freezing, these systems show relaxation behavior in this state. The rare earth transition metal pyrochlores ($Ln_2Ti_2O_7$) are example of frustrated systems [12].

1.1.2.3. Electrical properties:

Transition metal oxides show diverse electrical properties ranging from insulating to superconducting. This class of insulating materials mainly Mott insulators has become hot topic in condensed matter physics. On the other hand superconductive materials

belonging to this group started a new field of research. Other than many transition metal oxides are found to show ferroelectric and piezoelectric properties. So, electrical properties exhibited by this class of materials cover wide area of scientific research and worth studying.

Some of the oxides such as RuO_2, ReO_3 and $LaNiO_3$ are metallic in nature whereas some of manganites after doping with Ca, Sr, Ba or Pb in place of Lanthanum show insulator to metal transition owing to the presence of Mn in +3 and +4 state in the doping range $0.17< x <0.4$ in $La_{1-x}A_xMn_{1-x}Mn_xO_3$ and also exhibit ferromagnetism [11]. Owing to the strong repulsive interaction between electrons in transition metal ions in Oxides like Ca_2RuO_4 [15], Sr_2CuO_3, $SrCuO_2$ [16] and NiO etc. make these materials insulating. Apart from these, there are some materials like $BaTiO_3$, $PbTiO_3$, $LiNbO_3$ and $LiTaO_3$ can be used in capacitors. Rare earth chromites, $LnCrO_3$ (Ln = Ho, Er, Yb and Lu) are class of relaxor ferroelectrics, which show frequency dependent dielectric constants [17]. Lead Zirconate titanate, PZT is one of the famous piezoelectric materials that belongs to the family of transition metal oxides used actuators and sensors. Beyond these properties and phenomena, some of the materials exhibit coupling of magnetic and electrical properties and results in magnetoelectric or multiferroic materials.

Magnetoelctric Coupling: Magneto electric coupling is a coupling between magnetization and polarization or in other words induction of magnetization due to electric field and induction of polarization due to magnetic field. Magnetoelectric effect (ME) was first predicted by Curie in 1894 in some crystal considering crystal symmetry [19]. Later in 1960, magnetolecgric effect was conjectured theoretically in Cr_2O_3 and demonstrated by experimentally by Astrov and Rado [20-22] Magnetoelectric multiferroics have found applications in the field of memory devices. For practical applications, materials should have high value of coupling constant, spontaneous

polarization, and a good insulating behavior. Variety of mechanisms has been proposed to explain magnetoelectric effect or multiferroicity such as exchange striction, spin current model, p-d hybridization model [18] and so on. $RMnO_3$ ($R = Sc, Y, In, Ho, Er, Tm, Yb$) a class of compounds that show magnetoelectric effect.

Superconductivity: Certain materials below a paticular temperature, show superconducting transition which is characterized by two important properties; (i) zero electrical resistance and (ii) expulsion of magnetic field. In oxide systems, Bednorz and Muller discovered the phenomenon of superconductivity in 1986 in Copper oxide systems [23]. Since then, many superconducting oxide materials have been discovered in copper oxide family. $La_{2-x}Ba_x(Sr_x)CuO_4$ is a first a first copper oxide system found superconducting at 35 K [4]. Other copper oxide systems including $YBa_2Cu_3O_7$ (T_c=92 K), $La_2Ca_{1-x}Sr_xCu_2O_6$ (T_c=60 K), $TlSr_2Y_{0.5}Ca_{0.5}Cu_2O_7$ (T_c=90 K), $HgBa_2Ca_2Cu_3O_{8+\delta}$ (T_c=138 K) showed higher critical temperatures [4]. These systems find application in loss less electric power transmission, power storage devices and used as superconducting magnets in MRI.

1.2. High Pressure Science

For chemical reaction kinetics and equilibrium, pressure is an essential thermodynamic parameter. By the application of high pressures, atoms are forced into different geometries leading to the formation of crystal structures, which are unstable at ambient pressures and such materials can show interesting properties. High-pressure science covers many fields, from investigations into magnetic and electrical properties of materials in materials chemistry and fundamental properties of elements related to the geological and biological sciences [24]. In high pressure condensed matter physics, the latest inventions comprise the synthesis of high T_c superconductors, polymorphism and metallization of hydrogen. Specifically in the field of

superconductivity, contribution of high-pressure technology is remarkable. In copper oxide systems $HgBa_2Ca_2Cu_3O_{8+\delta}$ becomes superconducting at 138 K under a pressure of 30GPa without the change in phase [25-26]. Another record breaking high T_c superconductor H_2S which showed the superconducting property at 203 K under 150 GPa pressure [27]. In pharmaceuticals, the research in polymorphs of molecular crystals high-pressure synthesis is used.

1.2.1. Materials and aspects under High Pressure

High pressure studies on any material helps to explore those regions of the phase diagram which is not accessible at ambient pressure. The application of pressure to the material significantly increases the density and due to densification, the interatomic distance decreases and results in efficient packing of atoms and increases the coordination number of each atom. Also, decrease of interatomic distance may lead to the formation of material in different geometry and gives rise to new phase of the material. Diamond is the best example for a dense material made under high pressure. Main developments in high-pressure equipment occurred in mid of twentieth century due to keen interest of making diamond among researchers. Diamond is a kind of polymorph of carbon which is accessible at ambient pressure after high pressure synthesis but there are some polymorphs which are not accessible. e.g. sulphur. Materials like $LaFeO_3$, under ambient pressure and high temperature to form requires long time (more than 10 hr) but high pressure about 5GPa helps to prepare $LaFeO_3$ in five minutes. Hence, under high pressure due to increased contact between the grains and high ionic mobility helps in having increased reactivity and facilitates the kinetics of the reaction. Generally, high pressure reactions occur for few minutes or one to two hours rather than several days as in ambient pressure reactions. Since the atoms are quenched at high temperatures under high pressure, reaction may lead to the formation of metastable phase. There are some phases of materials in which transition metal ions can have

unusually high oxidation state. For example, $LaCuO_3$ where Cu is in +3 state [28] and in $SrCrO_3$, Cr is in +5 state [29].

List of materials transformed under high pressure [45, 46, 57] and corresponding change in coordination number is given below.

Material	**Structure at Ambient Pressure**	**Structure after High Pressure**	**Pressure applied(GPa)**	**Transition Temperature (^oC)**
Boron nitride	Graphite (3:3)	Sphalerite(4:4)	5	1500
SiO_2	Quartz(4:2)	Rutile(6:3)	12	1200
Carbon	Graphite(3)	Diamond(4)	13	3000
KCl	Rock salt(6:6)	CSCl-type(8:8)	2	RT
CdS	Wurtzite(4:4)	Rock salt(6:6)	3	RT
Li_2MnO_4	Phennacite(4:4:3)	Spinel(6:4:4)	1	400
$NaAlO_2$	Wurtzite(4:4:4)	Rock salt(6:6:6)	4	400
$(Mg,Fe)Si_2O_6$	Pyroxene(6:4:4)	Perovskite(8:6:6)	26	1600
$Na_2(Ti, Sn)\ TeO_6$	Ilmenite	Perovskite	7	950^oC

High pressure synthesis stabilizes materials by varying following parameters,

(a) Increase in coordination number (Dense packing of atoms): Na_2MTeO_6 ($M = Ti^{4+}, Sn^{4+}$) under ambient pressure adopts ilmenite structure whereas synthesis under high pressure of 7 *GPa* and high temperature of 950^oC makes it crystalize in perovskite structure which is known as most efficiently packed ternary oxide [30].

(b) High Oxidation state: Ambient pressure reaction of Calcium Oxide with Iron oxide leads to the formation of $CaFeO_{2.5}$ crystallizing in brownmillerite structure with Fe in +3 oxidation state

whereas the synthesis from same starting materials under high oxygen pressure with piston or belt type apparatus leads to the formation of $CaFeO_3$ with Fe in +4 state stabilized in perovskite structure [31].

(c) High symmetry: It is obvious that upon distortion the volume of polyhedron increases significantly. So, high pressures always favor symmetric coordination environments. As result of this, there won't be any shift in ferroelectric ion and suppression of stereo-active electron lone pair effects on $6s^2$ cations like Pb^{2+} , Bi^{3+}& Tl. For example, $PbSnO_3$, crystallizing in perovskite structure, is possible to synthesize under high pressure [32] whereas ambient pressure synthesis gives rise to mixture of PbO (owing to Pb^{2+} lone pair effect) and SnO_2.

1.2.2. History & Development in High Pressure Synthesis equipment

The application of temperature is comparatively straightforward than applying pressure on the sample because it needs very advanced techniques. Percy Williams Bridgman was the inventor of high-pressure synthesis technique and made great contributions to the scientific field in the mid of 20th century for which he received Nobel prize in 1946 [33]. There are two different techniques employed for high pressure synthesis of solids. i.e. dynamic compression and static compression. The former is based on shock waves and later uses pressure cells. In case of dynamic compression [34], the sample will be subjected to strong shock and velocities of shock waves be measured. Using this technique high pressure like 500-1000 GPa and high temperatures like tens of thousands of Kelvin can be reached. In static compression techniques, generally diamond anvils are used. Static compression technique is more accurate than dynamic but the maximum pressure attainable is comparatively less (around 300 GPa). In this case, laser heating can be used to attain the high temperatures [35]. Since, in the present study of materials static compression technique was used for synthesis and hence some of the

historical development on high pressure synthesis equipment for static compression has been discussed.

1.2.2.1. Opposed anvil device:

The inventor of high pressure physics, Percy Williams Bridgman has first designed opposed anvil device for measuring electrical resistivity at high pressure. This technique works on the principle of massive support [36]. By applying large load on large area called load face, high pressure is generated on small area called working area. There are two types in opposed anvil devices. (1) Bridgman opposed anvil device and (2) diamond anvil device.

Bridgman Opposed Anvil Device: This device consisting of opposed anvils made up of tungsten carbide, which is contained, in a shrunk-on steel ring.

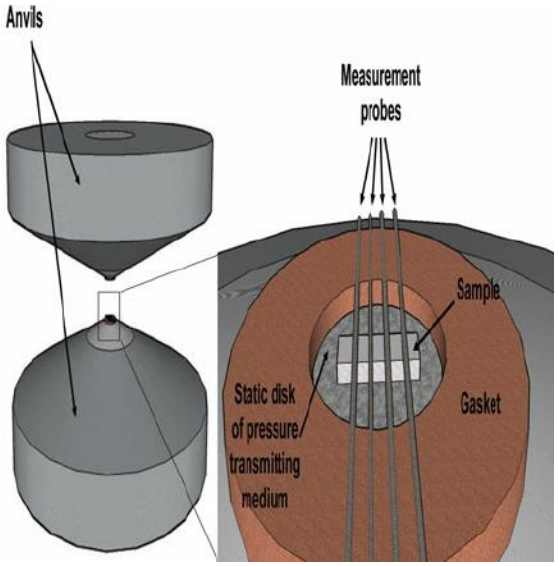

Fig.1.9. Design of Bridgman opposed anvil device [38]

The sample is covered with the silver chloride, which provides insulation and acts as pressure transmitting medium. This encapsulated sample is kept between flat, truncated faces of anvils. A ring of insulating pipe stone (catlinite) is surrounding the silver chloride encapsulated sample. Catlinite is a kind of clay, which is easily deformable after the application of load, but under

compression it becomes very strong in the direction perpendicular to that of compression. As a result it prevents lateral extrusion of encapsulated silver chloride. Since the materials used for encapsulation are insulating the electrical properties of the sample can be measured. Using this experimental high pressure design, Bridgman could achieve 10 *GPa* pressure [37].

Diamond Anvil Device: In 1954 after the successful synthesis of diamond by Hall [39], the anvils for high pressure equipment started making with diamonds as it is the only hardest material known among all, till now. Diamond anvil cell is a remarkable ultra-high-pressure device and many new states of matter have been found using it. This device could generate *GPa* of pressure. The device has designed such a way that the anvils are handy and much different kind of measurements can be done on materials of microscopic dimensions. It works on simple principle which can be expressed in terms of equation $P = F/A$ where P is pressure, F is applied force and A is area. Generally cullet size is in micron range, so very high pressure can be achieved my moderate amount of force on very small area.

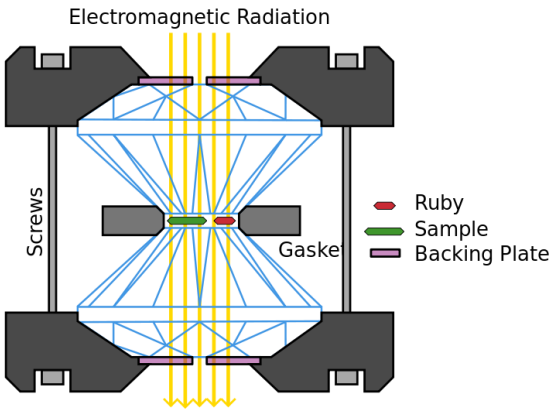

Fig.1.10. Design of Diamond anvil device [55]

In this technique, using a gasket the sample is placed between two flat-polished very high gem quality diamonds and the pressure is exerted on the sample by applying load. The

pressure exerted on the sample is monitored by using a material such as ruby, which is used as standard material for pressure calibration [40]. The uniaxial pressure exerted on anvils is converted into hydrostatic pressure using pressure transmitting media such as mixture of methanol and ethanol [41] or paraffin oil. These pressure transmitted medium are covered by gaskets. Generally gaskets are made of boron nitride [42] or tungsten. For lower pressure, steel can be used as gaskets as it's a commercially cheap material.

1.2.2.2. Multi Anvil Device:

Using this device the load can be applied on the sample from all other directions which prevents the extrusion of the transmitting medium, unlike Bridgman opposed anvil or diamond anvil device. This device consists of many anvils surrounding the sample cell and each anvil pointing inwards at the sample cell. Generally in multi anvil device two geometries are used. One is cubic anvil apparatus in which four anvils out of six of are arranged in the horizontal direction opposing at an angle 90°, and the remaining two anvils are arranged in the vertical direction enclosing a cubic volume [43]. Another device consists of eight anvils to compress sample in an octahedral geometry [44]. Both these devices make use of hydraulic press to drive the anvils and hence pressurize the sample.

In multi-anvil apparatus the compressed volume is called as "sample cell assembly". Depending on the temperature (T), pressure (P) condition and the type of experiment the sample cell assemblies vary in design and size. Sample cell assembly consists of a soft pressure medium in the shape of the volume enclosed by multi anvils in the apparatus, a furnace or a heater which converts AC or DC current into heat, a very soft confining media or the insulating material which can transmit the pressure to the sample and a sample jacket or encapsulating material that protects the sample from chemical reactions with encapsulated

materials. This design of sample cell assembly is mainly used for synthesis purpose. For measurements, it also can have thermocouple to measure the temperature and wires to measure the electrical properties of the sample.

Pressure Media: The pressure media is the principal element and plays significant role in the generation of high pressure. The shape of pressure media can be either cubic or octahedral and it should be of larger volume than the volume enclosed by anvils while touching.

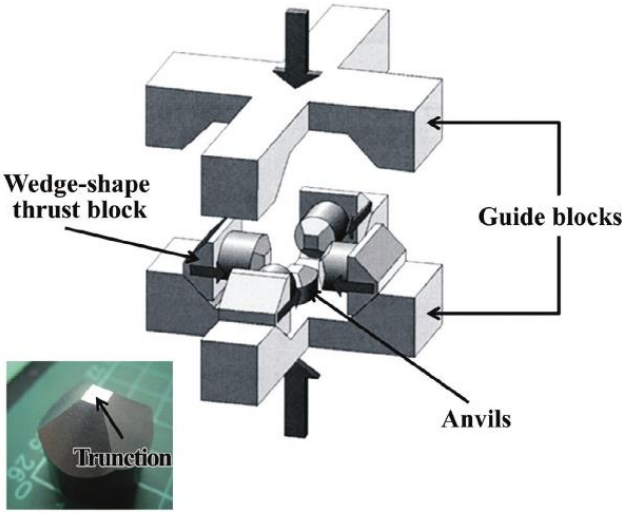

Fig.1.11. Design of cubic anvil device [56]

During the application of pressure using hydraulic press, the pressure media crushes out into the spaces between the anvils of the apparatus until the friction between the anvils and pressure media balances the pressure created inside the sample cell assembly. Hence material made of the pressure media must be soft enough to squeeze at room temperature but not very soft that it completely squeezes and breaks out between the anvils. It also serves as electrical insulating medium. The materials used as pressure media are pyrophyllite, mullite and boron epoxy.

Heater: Material used as furnaces should have high electrical resistance to heat the sample. It is also called as furnace. Heaters are generally in hollow cylindrical shape or a tube that touches the anvils through the conducting material. The current passing through the conducting material can be either DC or AC. At lower pressures generally graphite can be used as heater or furnace but at high pressures diamond can be used.

Confining Media: The confining media in the sample assembly act as pressure transmitting medium and it is situated next to the furnace. It avoids the direct contact of the sample jacket with the furnace and helps to distribute pressure from all the directions. Generally, the materials with high melting point, soft and chemically inert at high pressure and temperatures are used as confining media such as boron nitride, NaCl or magnesium oxide.

Sample Jacket: The sample jacket plays a significant role in high pressure synthesis. It avoids direct contact of the sample with the other elements of sample cell assembly and hence protects the sample from chemical reactions with them at high temperatures and pressures. Usually sample jackets are made of noble metals such as gold (Au) or platinum (Pt), which are chemically inert at high pressure and temperatures.

Sample: Sample is central part of the high pressure synthesis and it is the material being synthesized and studied. Most of the oxides and alloys are synthesized in multi anvil apparatus. Also it has some limitations such as volatile materials are difficult to confine and may diffuse during the course of experiments. However, during the synthesis of any material the excess oxygen can be provided by adding potassium chlorate, which serves as oxidant with reactants. Samples are mostly used in powder form in this type of synthesis.

1.3. Motivation

Present work reported in the thesis was motivated to explore corundum structures of $Ga_{1-x}Al_xFeO_3$(x=0, 0.5, 1) family of oxides under high pressure and high temperature. The orthorhombic structured $Ga_{1-x}Al_xFeO_3$(x=0, 0.5, 1) are well known oxides exhibiting novel magnetoelectric multiferroic properties [58]. The ball milling of these oxides lead to the structural transformation where $Ga_{1-x}Al_xFeO_3$ (x=0, 0.5) transforms directly from orthorhombic structure (*Pna2₁*) to rhombohedral structure (*R-3c*) while $AlFeO_3$ transform from orthorhombic structure (*Pna2₁*) to rhombohedral structure (*R-3c*) through intermediate crystal structure $P2_12_12_1$ formation. Such structural transformations are reasoned as local heating and pressure exerted on the particles due to friction during ball milling process [59]. Hence, high pressure synthesis of oxides with new structures will be having interesting properties which are worth exploring. Ternary oxides such as $AlCrO_3$ and $GaCrO_3$ found to crystallize in corundum type structure but proper study of structure and magnetic properties were not reported yet. Comparative study of magnetic properties of such $ACrO_3$ oxides with two different A cations will be interesting. Co in Y_2O_3.Co_2O_3 solid solution is found to exist with intermediate spin state [60]. Such unusual spin state of Co found great interest in the field of quantum mechanics and condensed matter physics. In this regard, IS state of Co in Lu_2O_3.Co_2O_3 and comparative magnetic study is performed under high pressure (~100 tons).

1.4. Bibliography

1. Physics of Transition Metal Oxides by Sadamichi Maekawa, Takami Tohyama, Stewart Edward Barnes (2004)
2. B. P. Mandal and A. K. Tyagi, *BARC NEWSLETTER,* **313** (2010)
3. Meagen A. Marquardt, Nathan A. Ashmore, David P. Cann, *Thin Solid films*, **496,** 146-156 (2006)
4. C. N. R. Rao and B. Raveau, Transition metal oxides, VCH Publishers Inc. (1995).
5. B. V. Beznosikov and K. S. Aleksandrov, *Crystallography Reports*, **45**, 792-798 (2000)
6. Tatsuya Takeguchi et al., *J. Am. Chem. Soc.*, ***135* (30)**, 11125–11130, 2013
7. Eylem, Cahit, et al. *Chemistry of materials* **4.5**,1038-1046(1992):.
8. M. A. Ruderman and C. Kittel, *Phys. Rev.* **96**, 99 (1954).
9. T. Kasuya, *Prog. Theor. Phys*. **16**, 45 (1956).
10. K. Yoshida, *Phys. Rev* **106**, 893 (1957).
11. A Anane et al., *Journal of Physics: Condensed matter,* **7(35)**
12. Greedan, John E, *Journal of Alloys and Compounds*, **444**, 408-412 (2006)
13. H. A. Jahn and E. Teller, *Proc. R. Soc.* A161, **220** (1937).
14. Midori Tanaka et al., *J. Phys. Soc. Jpn.* **21**, 262-267 (1966)
15. S Nakatsuji, *J. Phys. Soc. Jpn(* 1997)
16. Y. Taguchi et al., *Phys. Rev. B.*, **62**, 11-15 (2000)
17. Jyoti Ranjan Sahu et al., *J. Mater. Chem.*, **17**, 42-44 (2007)
18. Yoshinori Tokura et al., *Reports on Progress in Physics*, **77**, 7, (2014)
19. P. Curie, *J. Physique*, 3i`eme s'erie III (1894)
20. I. E. Dzyaloshinskii, *Zh. Exp. Teor. Fiz.* **37**, 881 (1959) [*Sov. Phys. JETP* **10**,628 (1960)].
21. D. N. Astrov, Sov. Phys. JETP **13**, 729 (1961).
22. D. N. Astrov, Sov. Phys. JETP **11**, 708 (1960).

23. Bednorz, J. G.; Muller, K. A.; Z. Phys. **1986**, B64, 187.

24. High-Pressure Synthesis of Electronic Materials by Penny, Edinburgh Research archive (2009)

25. P. Dai et al. *Physica C.* **243** (3–4), 201–206(1995)

26. L. Gao et al., *Phys. Rev. B* **50**, 4260 (1994).

27. Drozdov et al., *Nature*,**525**,73–76(2015)

28. G. Demazeau, C. Parent, M. Pouchard, and P. Hagenmüller, *Mater. Res. Bull.* **7**, 913(1972)

29. B. L. Chamberland, *Solid State Commun*. **5**, 663 (1967).

30. J.-H. Parka *J. Mater. Res.*,**14**(8)**,** 3192-3195(1999)

31. F. Kanamaru. Et al., *Materials Research Bulletin*, **5**(4), 257-261 (1970)

32. F Sugawara et al., *Materials Research Bulletin*, 3(6), 529-532 (1968)

33. http://www.nobelprize.org/nobel_prizes/physics/laureates/1946/bridgman-lecture.pdf.

34. J. W. Forbes. Shock wave compression of condensed matter: a primer. Springer, Berlin (2012).

35. A. Jayaraman. *Rev. Mod. Phys.*, **55,** 65 (1983).

36. M. Yousuf and K. Govinda Rajan, *Pramana*, **18**, 1-15 (1982)

37. P. Bridgman, *Proc. Roy. Soc. Lond. Math. Phys. Sci*. **203**, 1 (1950).

38. B. N. Bhavsar, A.R. Jani, *Journal of molecular crystals and liquid crystals*,**587**(1),121-128 (2013)

39. Hall, H. T, "The Synthesis of Diamond", J. Chem. Ed., **38**, 484-489 (1961)

40. Forman et al.,*Science*.**176** (4032): 284–5, (1972)

41. Jayaraman, *A. Reviews of Scientific Instruments.*, **57** (6), 1013, (1986)

42. Funamori, N; Sato, *The Review of scientific instruments*, **79** (5): 053903(2008).

43. https://en.wikipedia.org/wiki/D-DIA

44. http://serc.carleton.edu/NAGTWorkshops/mineralogy/mineral_physics/multi_anvil.html

45. A. R. West, Basic Solid State Chemistry (Wiley, 1999).

46. E. Ito and E. Takahashi, *J. Geophys. Res. B*, **94**, 10637 (1989).

47. http://www.cdti.com/spinel/ (copyright permission requested)

48. https://www.solarchoice.net.au/blog/news/perovskites-the-next-solar-pv-revolution-240714

49. J Awaka et al., *Journal of Physics and Chemistry of Solids*, **69**(7), 1740–1746 (2008)

50. T. M. McQueen et al., *J. Phys.: Condens. Matter*, **20**, 235210(2008)

51. AB Garg et al., *Journal of Applied Physics* **116**, 133514 (2014)

52. Guus Rijnders, *Nature Materials*,**13**,844–845(2014)

53. https://commons.wikimedia.org/wiki/File:Superexchange_in_MnO.jpg

54. Bettina Bechlars et al., *Nature Chemistry*,**2**,362–368(2010)

55.https://en.wikipedia.org/wiki/Diamond_anvil_cell#/media/File:Diamond_Anvil_Cell_-_Cross_Section.svg

56. Florian B. Hua et al., *Terrestrial Atmospheric and Oceanic Sciences*, **23**(6),647 (2012)

57. George B. S. Penny: High-Pressure Synthesis of Electronic Materials (2009)

58. Saha, Rana, et al. *Solid State Communications* 152.21 (2012): 1964-1968.

59. Saha, Rana, et al. *Inorganic chemistry* 50.19 (2011): 9527-9532.

60. Naidu, B. S., et al. *Chemical Physics Letters* 591: 277-281 (2014).

61. Zobel, C., et al. *Physical Review B* 66.2 (2002): 020402.

62. Dolphin, David H., John R. Sams, and Tsang Bik Tsin *Inorg. Chem* 16.3 (1977): 711-713.

63. Raveau, Bernard, and Motin Seikh. *Cobalt oxides: from crystal chemistry to physics*. John Wiley & Sons (2012).

Chapter 2

Experimental Techniques

2.1. Synthesis

Different kinds of techniques are in practice to synthesis the materials in solid state. Depending on the resources and the form of the material desired specific synthesis method can be employed. Generally methods such as solid state synthesis, sealed tube reaction, hydrothermal synthesis and sol gel synthesis and high pressure synthesis are adopted to prepare the material in solid state. Methods like sol gel and hydrothermal involves the use of solvents to carry out the reaction at low temperatures. Commonly sol gel method is used to get materials in nano form whereas hydrothermal synthesis helps to get single crystals. Most commonly alloys are synthesized under sealed tube conditions. High pressure synthesis is used to explore the materials with different phase which may be metastable. The most common method is solid state synthesis which is carried out generally at ambient pressure and high temperatures which gives product in polycrystalline form.

2.1.1. Ambient Pressure Synthesis

I. Solid state synthesis:

Solid state synthesis is the most commonly used synthesis method to get the compound in polycrystalline form. This method works on the principle of thermal diffusion. In this method the starting materials are ground finely and mixed properly. Then homogenously mixed powders are pressed in the form of pellets and heated. Generally grinding and mixing the materials are carried out in mortar and pestle. Intimate mixing and grinding the powders finely

results in formation of particles with small grain size having more contact than the coarse powder. The mixing and crushing of powders lead to formation of fine powder in macroscopic scale but on atomic scale the powders are still heterogeneous. So, to increase the efficiency of reaction, the powders are pelletized. Using the steel pellet die, the mixed powders are subjected to a load and pelletized in proper shape. Pressing the powders in the form of pellets increases the contact between the grains and helps in efficient reaction. These pelletized samples are placed in alumina crucibles and is heated at suitable high temperature in furnace for specific hours of time in order to get desired product. During the reaction, thermal diffusion occurs at the interface of two different reactants. At first, the reactants interact at the interface and the reaction takes long time to occur at the bulk of the grains. After each cycle of heating and cooling, the intermediate regrinding is carried out in order to redistribute the unreacted parts of the mixture.

During the course of reaction, a process called nucleation occurs followed by agglomeration to form the product. After mixing the powders homogenously, the diffusion or nucleation process doesn't occur this is because of lattice mismatch of the starting materials. For the process of nucleation to occur the energy should be supplied which helps to break the bonds of reactant molecule. This energy is supplied by heating the mixture at high temperatures. On heating, at particular temperature the bonds of the reactant molecule starts breaking and atoms migrate across the grain boundary to form the product which is process called diffusion.

Solid state synthesis can be carried out in box furnace or in tube furnace. Generally the reaction carried out in air done in box furnace and the reaction requiring particular gas atmosphere done in tube furnace. Also, solid state synthesis can be done in vacuum by using diffusion pump which can create dynamic vacuum so that it can drive out any gas evolved during the course of reaction.

II. Sol gel auto combustion synthesis:

This is most efficient low cost solution based method which needs low temperature for product formation. It is basically known as solution-gelation auto combustion method which involves the dissolution of starting materials (metal nitrates) in appropriate solvent (water) leads to the formation of gel upon heating at low temperatures (80-90^{o}C). Auto combustion method mainly requires fuel which also acts as complexing agent. Upon dissolution of reactants in appropriate solvent it gives rise to ions in the solution and well mixed with each other. This is most efficient method than solid state synthesis because it results in atomic level mixing of reactants. Since it needs very low temperature for product formation, hence it is cost efficient. Usually the starting materials used are metal nitrates and citric acid as fuel. It yields the product with high purity. Mostly, nanoparticles are synthesized using this method.

It works on the principle of gel formation and auto combustion of an aqueous solution containing nitrates using the complexing agent and fuel, citric acid. Other than citric acid, urea can also be used as fuel [1]. In this synthesis, first metal salts (generally nitrates) in appropriate stoichiometric ratio, are dissolved in deionized water to prepare homogenous solution. Then the fuel is added and dissolved in the aqueous solution. Generally fuel of twice the moles of cationic precursor is added for efficient gel formation and auto combustion process. Then the Solution is heated at 80-90^{o}C with continuous stirring on heating mantle until it evaporates to form viscous gel. The resulted gel is then heated in oven at temperature equal to the flash point of the fuel for several hours. For citric acid, the flash point is 200^{o}C. Upon heating in oven the resulting porous compound is ground in mortar and pestle homogenously resulting in fine powder and heated at 600^{o}C for several hours in oxygen atmosphere to remove the carbon residue as CO_2.

2.1.2. High Pressure Synthesis

History of high pressure synthesis started from making diamond out of carbon based material graphite. In 1946, for the first time P.W. Bridgman built an opposed anvil device made of tungsten carbide anvils and opened an era of high pressure technology. Using high pressure synthesis, materials with high oxidation state, controlled composition and metastable phases which cannot be synthesized under ambient pressure conditions are prepared. Even if this method is expensive and gives product in small scale, it has its unique advantages that can't be accomplished by any other method. In the present study of transition metal oxides, the materials are prepared under high pressure using multi anvil device namely cubic anvil apparatus. The geometry of the volume enclosed by the anvils is in cubic shape. So, it is named as cubic anvil apparatus.

The whole apparatus consists of assembled anvils in cubic geometry and hydraulic press to apply the load. The anvils are made of tungsten carbide which is the hard and dense material with density 15.6g/cm^3. In many high pressure equipments, other than diamond, tungsten carbide is used to make anvils because it can sustain high compressive stress of low cost compared to diamond. There is a digital pressure controller which shows the value of the load applied on the sample cell assembly. It also has digital power controller which shows the value of power supplied for resistive heating of the sample. Apart from this, sample cell assembly is the heart of high pressure synthesis. In the present study, the basic elements of sample cell assembly involve pressure transmitting media, Confining media, heater, sample jacket and sample.

Pressure Transmitting Media: In the present work, pyrophyllite of dimension 15mm x 15mm x 15mm with a hole of diameter 8mm is drilled through one pair of faces. Pyrophyllites are

compound with chemical formula $Al_2Si_4O_{10}(OH)_2$. Before using the pyrophyllites for synthesis it should be preheated at certain temperature to remove any moisture or water of crystallization.

Heater: Here, graphite cylinder with two enclosing lids is used as a heater or furnace during synthesis. Graphite cylinder is of height 9 mm and inner and outer diameter 6.7mm and 8mm respectively. The graphite lids are of 0.66mm thickness and diameter 6.7mm.

Confining Media: Sodium chloride (NaCl) with 20 wt.% zirconium oxide (ZrO_2) is used as confining media which separates the sample jacket from the heater. The confining media is in the form of closed hollow cylinder consisting of (NaCl+ZrO_2) sleeve and the two disks to enclose the sleeve. Sometimes, BN can also be used as confining media.

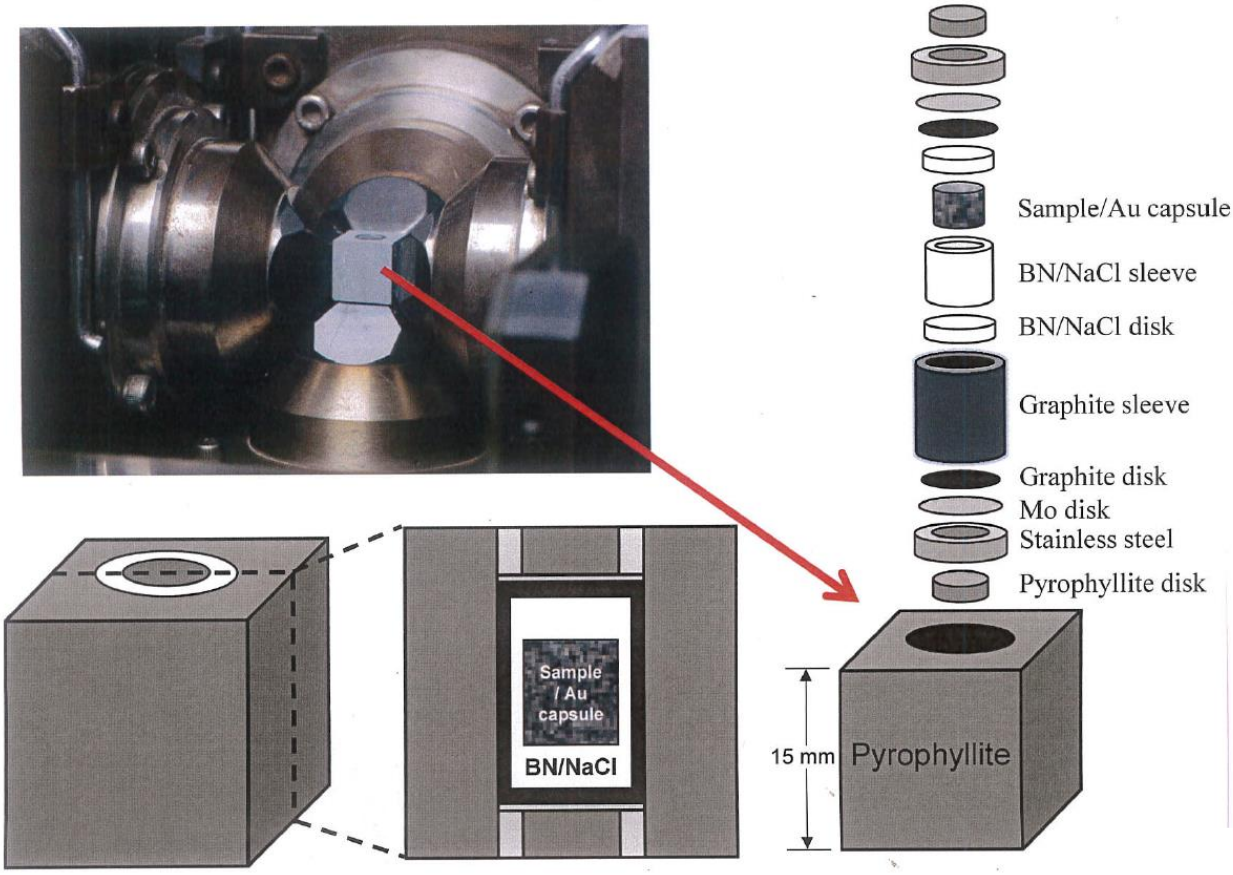

Fig.2.1. Schematic of entire sample cell assembly

Sample Jacket: Gold capsule is used as a sample jacket to protect the sample from any chemical reactions with the other elements of sample cell.

Sample: Sample is the central part of the cell assembly. It is in the form of solid cylinder of 0.5mm diameter and 0.5mm height.

Apart from these, there are some elements which complete the sample cell like Mo plate which conducts electricity to graphite. Also, there are two pyrophyllite disks with stainless steel ring surrounds it on each side of the pyrophyllite hole. The stainless steel passes on the electricity provided by the power supply to Mo plate.

Pressure Calibration Method: The load applied by the hydraulic press on a certain area of the pressure transmitting media (pyrophyllite) is experienced as pressure of some value. Pressure values vary slightly in different region of pyrophyllite. So to quantify the actual pressure generated precisely at the center of the pyrophyllite (sample's position) the pressure has been calibrated using bismuth metal. Bismuth shows a structural transition from phase I to II at 2.55GPa [10].

Procedure:

1. The center of the transverse faces of the pyrophyllite (15mm X 15mm) is marked and a hole of diameter~1.5mm is bored at marked position.

2. An insulation tube is inserted through these boreholes to protect the lead wires (measuring leads) passing through it.

3. The bottom half of the pyrophyllite is filled with stainless steel ring surrounding the pyro lid, Mo plate, graphite lid, graphite heater containing NaCl+ZrO_2 disk in the order. The upper half of the pyrophyllite is also filled in same manner.

4. The bismuth metal is placed between two NaCl+ZrO_2 disks and the lead wires are arranged such a way that it should be in proper contact with the Bi metal as shown in the Fig.2.2.

5. The anvils surrounding the pyrophyllite cube are kept in contact with the lead wire on the face of the pyrophyllite and precaution has to be taken so that no two anvils touch each other.

6. A constant current source is connected to one pair of anvils and the resulting voltage is measured by voltmeter connected to another pair of anvils. By noting down voltage and constant current values resistance is calculated.

7. The graph of resistance calculated against load applied (in tons) shows the structural transition of Bi I → II around 2.55GPa.

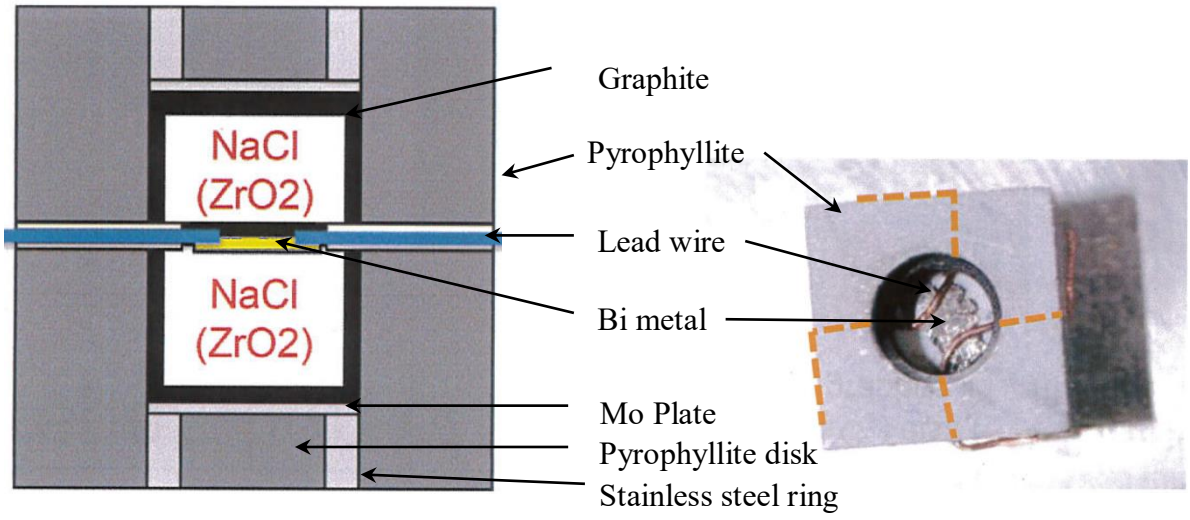

Fig.2.2. Schematic design (left) and Photographic image (right) of sample cell during pressure calibration

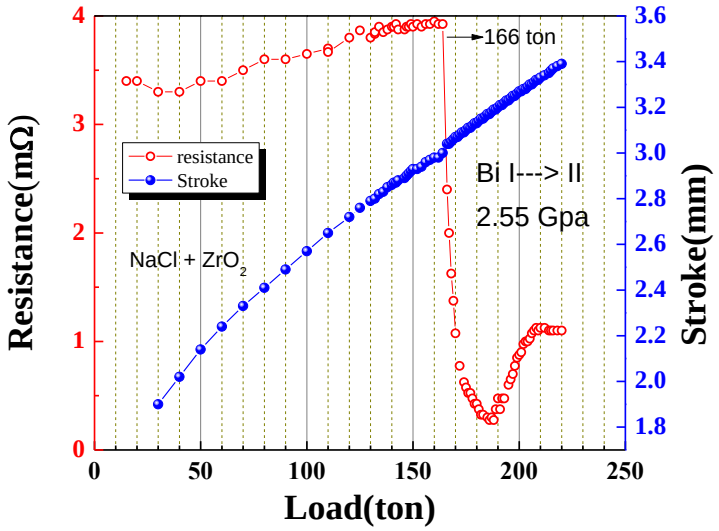

Fig.2.3. Pressure calibration graph of Japanese pyrophyllite

The high pressure equipment used in the present work can apply maximum load pressure calibration graph is shown in the Fig.2.3.

Temperature Calibration Method: The high pressure equipment has provided with 2kW power supply which shows the power supplied for heating the sample during synthesis on digital meter but there is no thermal meter which shows the temperature of the sample directly. So, to determine the power–temperature relationship, the temperature calibration experiment has been done.

1. The center of the any two opposite transverse faces of the pyrophyllite (15mm X 15mm) is marked and a hole of diameter ~ 1.5mm is bored at the marked position.

2. An insulation tube is inserted through these boreholes to protect the thermocouple of K type leads passing through it.

3. The bottom half of the pyrophyllite is filled with stainless steel ring surrounding the pyro lid, Mo plate, graphite lid, graphite heater containing NaCl+ZrO_2 disk in the order. The upper half of the pyrophyllite is also filled in same manner.

4. The thermocouple contact point is placed between two NaCl+ZrO_2 disks as shown in the Fig.2.4.

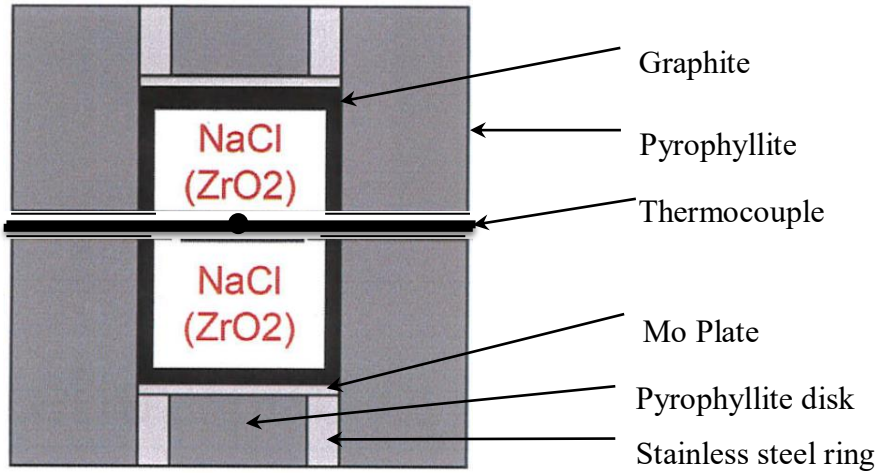

Fig.2.4. Schematic Design of sample cell for temperature calibration

5. The leads are connected to the digital thermal meter.

6. Under 250 tons load, the pyrophyllite is heated by supplying the power at constant rate and maintained at 860 W for 1 hour. During the experiment, the power value and the temperature from digital thermal meter is noted down.

7. Graph of temperature against power supplied is plotted which gives Temperature-Power relationship as shown in the Fig.2.5.

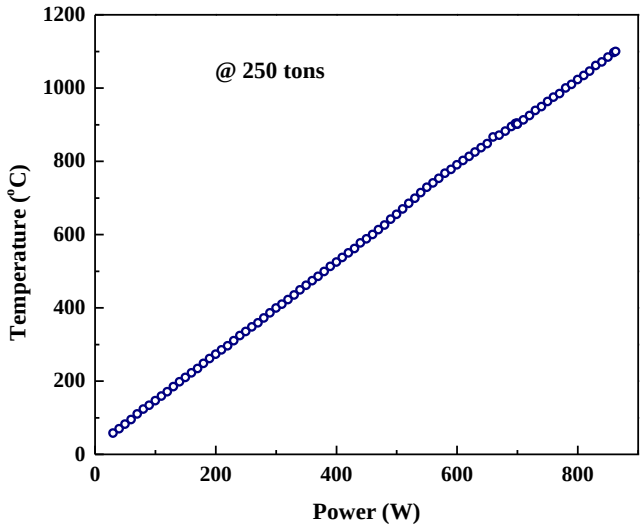

Fig.2.5. Temperature calibration graph of Japanese pyrophyllite

2.2. Crystal structure Analysis and Techniques

I. X-ray Diffraction

X-ray diffraction is an analytical technique to find the crystal structure of solid compounds. After the discovery of x-rays by Wilhelm Rontgen in 1901, von Laue has observed the diffraction of X-rays by crystals in 1912. He found that the interatomic planes in the crystal act as three dimensional diffraction grating since x-ray wavelength is comparable to interatomic distance. This technique works on the principle of constructive interference between X-rays diffracted from crystalline planes. At first the cathode ray tube generates the x-rays which are then passed through monochromator to get the X-rays of single wavelength. Then it is collimated and concentrated towards the sample. Only those diffracted X-rays results in constructive interference which obeys Bragg's law, $n\lambda = 2\,d\sin\theta$. Such diffracted X-rays detected using the detector, processed and counted. The sample is scanned through 2θ angles to consider all random orientation of atomic planes.

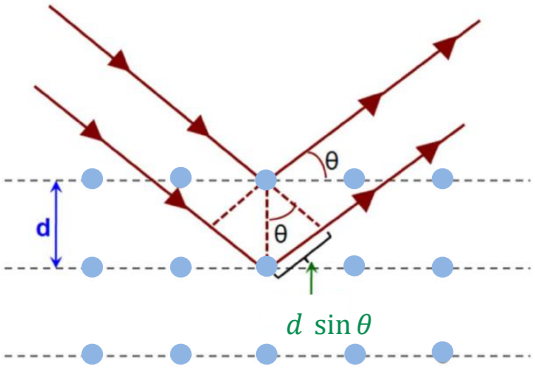

Fig.2.6. Bragg Diffraction Geometry

Each compound has its unique structure with specific interatomic planes. Hence X-ray diffraction pattern is characteristic of the crystal structure of particular compound. Using X-ray diffraction pattern, particle size of the crystal can also be determined. The X-ray diffraction pattern obtained has series of peaks whose shape is combination of Gaussian and Lorentzian function. A good crystalline material will have sharp and high intense peaks in its diffraction pattern and such patterns are very good for crystal structure refinement. In present thesis, the X-ray diffraction data for the samples were recorded in PANalytical Empyrean single wavelength ($K_{\alpha 1}$) diffractometer.

II. Neutron Diffraction

Neutron diffraction is another important analytical technique to find the crystal structure of the sample. In addition to atomic crystal structure it is mainly used for the magnetic structure determination. In this thesis, neutron diffraction data is used to find the atomic crystal structure. The neutron diffraction data is collected in constant wavelength mode. Neutrons are generated using spallation sources and reactors. In case of reactors, the neutrons are produced by nuclear fission of heavy nucleus ^{235}U, whereas in spallation source, the high energy protons produced by particle accelerator bombard the metal target. Due to the collision very high energy

is imparted to the target and generates the spallation neutrons. Since such neutrons have high energy it will be passed through moderator, heavy water to decrease the energy and further used for diffraction data collection of the sample. While collecting diffraction data in constant wavelength mode, Debye Sherrer diffraction geometry is employed and there will be series of detectors which are allowed to move around the sample. Using an appropriate monochromator the single wavelength neutron beam is used during diffraction data collection of the sample.

III. Rietveld refinement

Rietveld refinement is a crystal structure refinement method used for the analysis of X-ray and neutron powder diffraction [2, 3]. Basically it makes use of least square fitting method that involves the minimization of difference between experimental and calculated diffraction profiles. It is the least squares fitting procedure that minimizes the difference between the observed and calculated diffraction profiles. The least-squares parameters used in the refinement are of two types i.e. one is instrumental parameters and another is structural parameters. The instrumental parameters include the asymmetry correction, zero offset, the peak shape parameters, the background parameters, and absorption correction. The structural parameters include lattice parameters of the unit cell, scale factor, the atomic coordinates and thermal parameters of each element forming the asymmetric unit. During the Rietveld refinement, the profile function (peak shape function) used is Pseudo Voigt. This is close approximation of Voigt function. Pseudo Voigt (ηV) is convolution of Gaussian (G) and Lorentzian (L) function which is given by following equation [4],

$$pV = \eta L + (1 - \eta)G$$

Where, η is the Pseudo-Voigt convolution parameter. The equation [5] correlating the angle (2θ) with the full width at half maximum ($FWHM$) of Gaussian and Lorentzian component of profile function can be given as,

$$(FWHM)_G^2 = U\ tan^2\theta + V\ tan\ \theta + W$$

$$(FWHM)_L = X\ tan\theta + Y/cos\theta$$

Where U, V and W are the Gaussian component of $FWHM$ parameters, and X, Y are the Lorentzian component of $FWHM$ parameters.

In Rietveld refinement there are 3 main steps. (i) pattern matching (ii) atom refinement and (iii) bond refinement. In the step of pattern matching the zero offset and possible lattice parameters, U, V, W, shape and asymmetric parameters are refined iteratively by giving appropriate space group. In the step of atom refinement, scale factor, atomic coordinates, thermal parameters and occupancy values are refined iteratively. In the bond refinement, the bond lengths are calculated.

In Rietveld refinement the well fitted profile must have chi squared value near to 1. This value is known as goodness-of-fit (GOF) and it can be expressed as,

$$\chi^2 = \frac{R_{wp}}{R_{exp}}$$

Where, R_{wp} is difference between weighed and profile R-factors and R_{exp} is the expected R-factor after profile fitting and are given by the equations [6],

$$R_{wp}(weighed - profile) = \{\frac{\sum_i w_i\,[y_i(obs) - y_i(calc)]^2}{\sum_i w_i[y_i(obs)]^2}\}^{1/2}$$

$$R_{exp}(expected) = \left[\frac{(N-P)}{\sum_i^N w_i y_i(obs)^2}\right]^{1/2}$$

Where $y_i(calc)$ and $y_i(obs)$ is the calculated and observed intensity at step i respectively and w_i is the weight given to the individual step intensity. N is the number of observations and P is the number of refinable parameters. Ideally for a good refinement χ^2 should approach 1.

2.3. Magnetic Property Measurements

2.3.1. DC Magnetic Measurements

There are different types of magnetic materials which can show different behavior in external magnetic field. This mainly depends on the presence of unpaired electrons in their valence shell and electron's spin alignment. Depending on the responses showed by the materials in external magnetic field, they can be classified as ferromagnetic, antiferromagnetic, paramagnetic, diamagnetic and ferrimagnetic. Ferromagnetic materials are the one which shows strong attraction with the external magnetic field and retain the magnetization even after the removal of external magnetic field. They possess high positive magnetic susceptibility. They possess domains of spins where the spins are aligned parallel to each other resulting in high magnetic moment along particular direction. Antiferromagnetic materials also have unpaired electrons in their outer electron shell but they align antiparallel to each other resulting in zero net magnetization. Ferrimagnetic materials are a type of antiferromagnetic materials which have alternating spin but the opposite spins are of different moments giving rise to net non-zero magnetic moment. Paramagnetic materials are another class of materials having unpaired electrons in outer most shell and in the presence of magnetic field, it attains net magnetic moment but it doesn't retain the magnetization after removing the field. These materials possess very small positive magnetic susceptibility. Diamagnetic materials do not have any unpaired electrons and they get repelled by the magnetic field. They possess negative magnetic susceptibility.

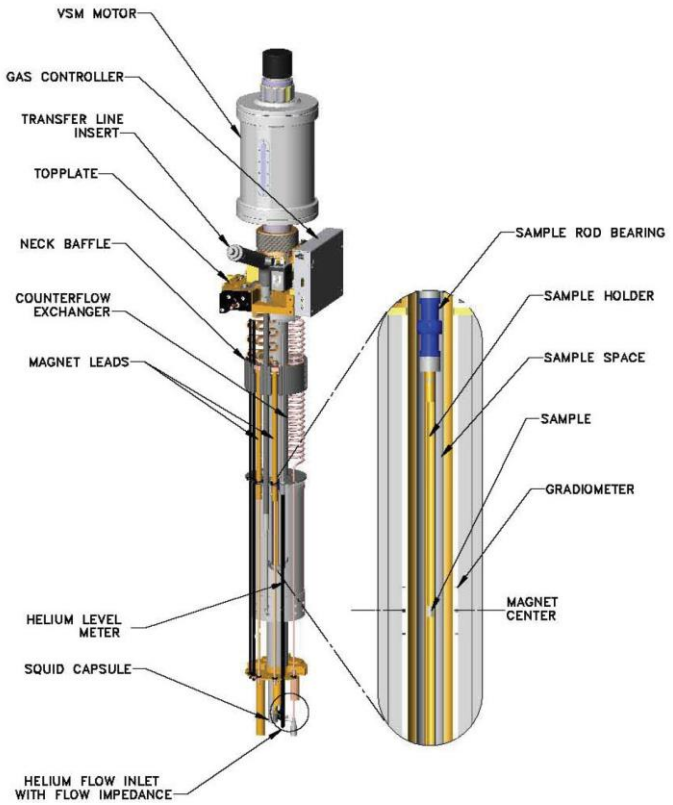

Fig.2.7. Schematic diagram of SQUID VSM system and Probe [8]

All the low temperature magnetic measurements reported in the thesis is carried out using SQUID (Superconducting Quantum interference Device) - VSM (Vibrating Sample Magnetometer) MPMS3 (Magnetic Property Measurement System). A SQUID magnetometer consists of superconducting magnet, detector coil and helium cryostat. The helium gas is used to maintain the sample temperature and helps to attain lowest temperature 4 K. The detector in the SQUID magnetometer has a Josephson junction loop situated inside the apparatus. The detector is exposed to magnetic field created by superconducting magnet and moved through the pick-up coil arrangement. The pick-up coil is induction coil with upper and lower turns counter wound with two turn center coil [7].This arrangement of coils avoids interference of any other magnetic field in vicinity. When the sample is vibrated through the pickup coil, the magnetic moment of

the sample induces change in the magnetic flux which according to Faraday's law induces change in electric current in the coil. Thus, the voltage induced in the pickup coil is directly proportional to the magnetic moment of sample which can be given by the equation,

$$V_{coil} = 2\pi f C m A \sin(2\pi f t)$$

Where, C is the coupling constant, m is the magnetic moment of the sample, f and A are the frequency and amplitude of the vibration.

Procedure of magnetic measurement in SQUID: The SQUID sample holder consists of a quartz rod on which sample is mounted at the center of the rod with the help of stand with the mirror using teflon. The sample probe connecting the sample holder is put inside the SQUID sample chamber. While carrying out high temperature magnetic measurements the sample is mounted on the holder using adhesive named ZIRCAR cement. There are two different methods of carrying out magnetic measurement. One is measurement of magnetic moment of the sample with respect to change in the temperature by applying DC magnetic field. This is called DC magnetization measurement. There are two different ways of doing it. One is field cooled (FC) DC magnetization measurement in which sample is cooled to low temperature in the presence of certain field and the magnetic moment data of the sample s collected while warming in the presence of field. Another way is Zero field cooled DC magnetic measurements in which the sample is cooled to low temperature and the magnetic moment data of the sample is collected during warming in the presence of the field. Another method is measurement of magnetic moment of the sample with respect to magnetizing field at constant temperature which gives rise to M-H loop of the sample.

2.3.2. AC Magnetic Measurements

AC magnetic moment of a sample is dynamic magnetic moment and is time dependent because the magnetization of the sample is studied in the presence of applied alternating magnetic field, $H_{ac} = H_o \sin \omega t$, where ω is the frequency of the applied field. While carrying out AC magnetic measurement, no need to vibrate the sample as in DC magnetic measurements because AC field induces itself induces a current in the coil due to electromagnetic induction. In DC magnetic measurement, magnetic moment of the sample (m) is measured which is used to calculate magnetic susceptibility $\chi = \frac{M}{H}$ where, M is magnetization of the sample and H is magnetizing field. In AC magnetic measurements, $\chi = \frac{dM}{dH}$ is measured since the field applied is varying with time. AC magnetic susceptibility measured with the field of low frequency is almost similar to the DC magnetic susceptibility data. AC magnetization, M_{AC} measured in presence of small AC field, H_{AC} can be given by the equation,

$$M_{AC} = \left(\frac{dM}{dH}\right) \cdot H_{AC} \sin(\omega t)$$

Where, ω and H_{AC} is the frequency and amplitude of the applied AC magnetic field, $(\frac{dM}{dH})$ is the AC magnetic susceptibility of the sample. AC magnetometry is very sensitive tool which can measure very small change in magnetic moment of the sample. For the AC magnetization measurements at high frequencies the AC magnetization of the sample lags behind AC magnetizing field by a phase φ. Hence the resulting magnetic susceptibility of the sample consist of two parameters i.e. in-phase component of magnetic susceptibility, χ' and out-of phase component of magnetic susceptibility, χ'' . Hence AC magnetic Susceptibility at frequencies can be given by the equation,

$$\chi = \chi' + j\chi''$$

Here, $\chi'$is real component of χ and χ'' is imaginary component of χ.

$$\text{Also, } \chi' = \chi \cos\varphi \text{ and } \chi'' = \chi \sin\varphi$$

$$\chi = \sqrt{\chi'^2 + \chi''^2}\ ;\ \varphi = \tan^{-1}\left(\chi''/\chi'\right)$$

In case of AC magnetic measurement carried out at low frequency field, χ' is slope of the M (H) curve obtained by DC magnetic measurement. Mainly χ'' indicates the loss in the sample. Generally spin glasses are characterized by this technique and spin glass systems give rise to non-zero χ'' because of the loss occurred during magnetic relaxation and irreversibility. Generally, such losses results due to eddy current generation.

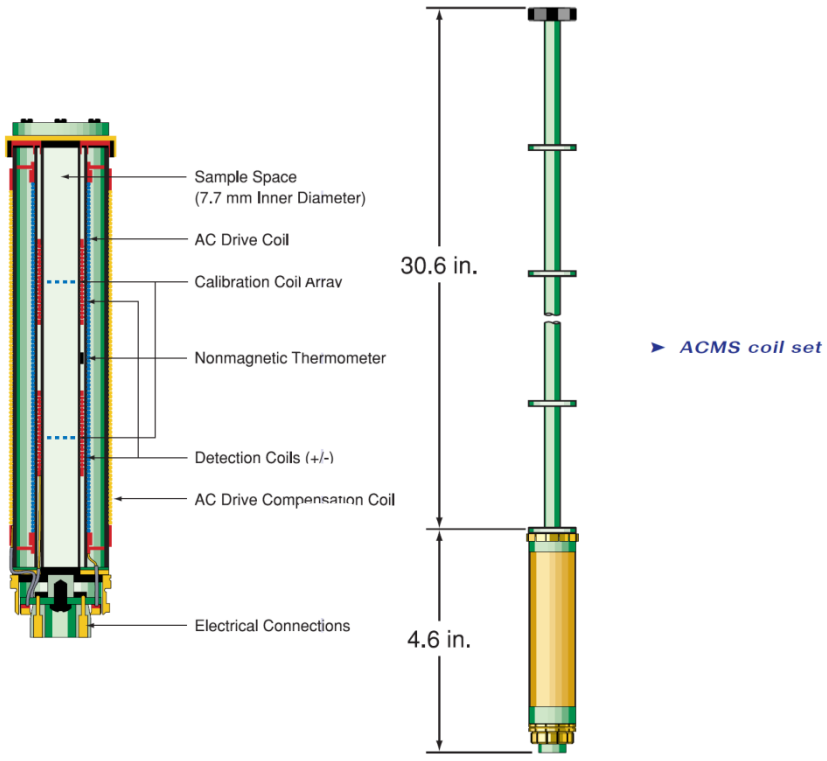

Fig. 2.8. Schematic diagram of PPMS system and Probe [9]

In this thesis, the AC magnetization measurements are carried out to characterize the spin glass system. Using this technique the shift in freezing temperature of the spin glass system has been observed. The AC magnetization measurements are carried out in PPMS (Physical Property Measurement System). The magnetometer consists of three different coils i.e. one primary coil which generates the AC magnetic field and two secondary coils. The sample is kept at the center of one of the secondary coils and coils are wound so that any signal generated by the coils gets cancelled out. Two components of susceptibility are collected by lock-in amplifier circuit. During the measurement, the sample is moved once to the center of bottom detection coil and then to center of the top detection coil. Thus obtained signals are modified using analogue to digital converter. The data is saved as a waveform. Using these waveforms, the real and imaginary part of χ is calculated.

2.4. Second Harmonic Generation Experiment

Second harmonic generation (SHG) is a very useful technique to verify the existence of center of symmetry in the crystals. Generally, materials which are non-Centro symmetric exhibits piezoelectric property, thus using SHG the existence of piezoelectricity in the crystal can be determined [11]. In this technique, a high intense laser light of particular wavelength (λ) is passed through non centro-symmetric crystal which generates the laser light of half the incident or doubles the frequency of incident light as shown in Fig.2.9. This process is also called as frequency doubling. Here, the incident optical wave of frequency f gets added with itself after passing through non centrosymmetric crystal medium and give rise optical wave of frequency 2 f.

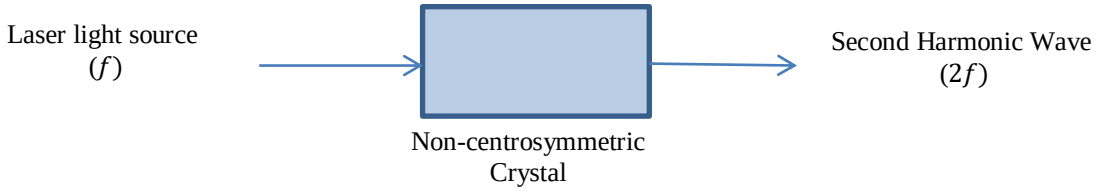

Fig. 2.9. Schematic diagram of Second harmonic Generation

Generally, Nd-YAG (Neodymium doped Yttrium Aluminum Garnet) laser of λ,1064 nm is used as source for this measurement. Upon SHG, resulting output appears as a green laser light of λ, 532 nm. In the present thesis, to verify the absence of inversion center in the polycrystalline compound, SHG experiment has been carried out.

2.5. Bibliography

1. H Fang, L. Wang, *Front. Chem. China*, **3**,193 (2008)
2. H. M. Rietveld, *J. Appl. Crystallogr*. **2**, 65 (1969).
3. H. M. Rietveld, *Acta Crystallogr*. **22**, 151 (1967).
4. P. Thompson, D. Cox, and J. Hastings, *J. Appl. Crystallogr*. **20**, 79 (1987).
5. G. Caglioti, A. t. Paoletti, and F. Ricci, *Nuclear Instrum*. **3**, 223 (1958).
6. L. McCusker, R. Von Dreele, D. E. Cox, D. Louer, and P. Scardi, *J. Appl. Crystallogr*. **32**, 36 (1999).
7. The measurement, instrumentation, and sensors handbook. 32-113(1999).
8. http://physique.umontreal.ca/~andrea_bianchi/uploads/Site/SQUID_VSM_User_Manual.pdf
9. http://www.qdusa.com/sitedocs/productBrochures/mag7-16.pdf
10. Dekker D L, Bassett W A, Merrill L, Hall H T and Barnett J, *J. Phys. Chem.* Ref. Data 1, 827(1972)
11. Robert C. Miller, *Appl. Phys. Lett.* **5**, 17 (1964)

Chapter 3

High Pressure Synthesis and Study of $Ga_{1-x}Al_xFeO_3$ family of oxides

Summary

New phases of oxides $GaFeO_3$ and $Ga_{0.5}Al_{0.5}FeO_3$ were prepared under high pressure (4.5 *GPa*) and high temperature (1000 °C) using wedge-type cubic-anvil high pressure apparatus. X-ray diffraction studies showed that application of pressure transform the structure of $GaFeO_3$ and $Ga_{0.5}Al_{0.5}FeO_3$ from $Pna2_1$ (non-centrosymmetric) to *R-3c* (centrosymmetric) phase. Both oxides $GaFeO_3$ and $Ga_{0.5}Al_{0.5}FeO_3$ show antiferromagnetic ordering but with different Neel temperatures i.e. at T_N = 450 K and T_N = 650K, respectively. M-H hysteresis loop at 300K indicates the presence of spin canting in both oxides below T_N. Magnetic studies on $GaFeO_3$ and $Ga_{0.5}Al_{0.5}FeO_3$ shows a bifurcation of FC and ZFC curves at T = 45 K and T = 43 K respectively. Frequency dependent ac susceptibility shows peak shift indicating the presence of spin glass state at low temperatures. The ac susceptibility measurements are analyzed using Vogel Fulcher law and other theoretical models explaining critical slowing down behavior of cluster spin glass state at low temperature. This behavior can be understood based on cation site disorder between the antiferromagnetically interacting Fe^{+3} ions in octahedral site of the corundum structure. Intriguingly, it is found that the ambient pressure synthesized orthorhombic $AlFeO_3$ decomposes into its constituent oxides, Al_2O_3 (*R-3c*) and Fe_2O_3(*R-3c*) under high pressure (~4.5 *GPa*) and high temperature (~ 1000^{o}C).

3.1. Introduction

Binary oxides such as α-Al_2O_3 and α-Fe_2O_3 crystallize in corundum structure with the space group *R-3c* whereas β-Ga_2O_3 crystallizes in monoclinic crystal structure with space group *C2/m*. The ternary oxides $AlFeO_3$ and $GaFeO_3$ synthesized at high temperature and ambient pressure using α-Al_2O_3 (β-Ga_2O_3) and α-Fe_2O_3 resulted in a chiral orthorhombic crystal structure with space group $Pna2_1$ which is different from crystal structure of parent oxides [1-2]. $AlFeO_3$ and $GaFeO_3$ are well known magneto-electric below their Neel temperatures, T_N=210 K and 250 K, respectively [1-2].

Upon ball milling, these oxides show structural phase transformation from non-centrosymmetric to centrosymmetric crystal structure. $AlFeO_3$ transform from orthorhombic structure (*$Pna2_1$*) to rhombohedral structure (*R-3c*) through an intermediate orthorhombic phase (*$P2_12_12_1$*) whereas $GaFeO_3$ directly transforms from orthorhombic structure (*$Pna2_1$*) to rhombohedral structure (R-3c) [3]. Similarly, the mixed compound, $Al_{0.5}Ga_{0.5}FeO_3$, upon ball milling, transform from the chiral orthorhombic crystal structure to *R-3c* without any indication for intermediate *$P2_12_12_1$* phase formation. Upon ball milling the magnetic transition temperature of oxides in *R-3c* structure are increased compared to that of *$Pna2_1$* structure. These oxides upon heating to high temperature converted back to stable orthorhombic structure (*$Pna2_1$*). These metastable phases of oxides are stabilized due to local heating and pressure on the particles due to friction during ball milling.

On account of these phase transformations of $GaFeO_3$, $Al_{0.5}Ga_{0.5}FeO_3$ and $AlFeO_3$ due to ball milling, to understand the pressure effects on these ferrites, high pressure synthesis and properties of resulting compounds have been studied.

3.2. Scope of the investigation

This chapter mainly focuses on the high pressure synthesis and study of $Ga_{1-x}Al_xFeO_3$ (x=0, 0.5). The presence of elusive cluster spin glass systems in these oxides has added two more systems in the group of disordered magnetic systems and hence significant in studying off equilibrium behavior. This class of systems emerged with new ideas to understand other complex systems like colloids, neural networks and granular materials. Also, the decomposition of $AlFeO_3$ into constituent oxides Al_2O_3 and Fe_2O_3, a rare phenomenon observed in high pressure research, is reported.

3.3. Experimental Details

3.3.1. Synthesis

$GaFeO_3$ and $Ga_{0.5}Al_{0.5}FeO_3$ are synthesized by heating the corresponding oxides under high pressure and high temperature. While synthesizing $GaFeO_3$, the stoichiometric amounts of constituent oxides β-Ga_2O_3 (99.9%) and α-Fe_2O_3 (99.9%) in powder form are mixed thoroughly using mortar and pestle to make homogenous fine powder. This mixture is used as starting material for the $GaFeO_3$ synthesis. In case of $Ga_{0.5}Al_{0.5}FeO_3$, using solid state method the starting material $Ga_{0.5}Al_{0.5}FeO_3$ in orthorhombic (*Pna2₁*) phase is synthesized and used it as starting material for high pressure synthesis. During solid state synthesis of $Ga_{0.5}Al_{0.5}FeO_3$, the constituent oxides, α-Al_2O_3 (99.9%), β-Ga_2O_3 (99.9%) and α-Fe_2O_3 (99.9%) in powder form are mixed and powdered thoroughly using mortar and pestle to make homogenous fine powder. This mixture is heated at 1400°C at 5°C/min heating rate in the furnace with repeated grinding, pelletizing and heating. Thus formed $Ga_{0.5}Al_{0.5}FeO_3$ crystallizes in orthorhombic *Pna2₁* phase. This is used as

starting material for high pressure synthesis of $Ga_{0.5}Al_{0.5}FeO_3$. The high pressure reaction is carried out under a wedge-type cubic-anvil high pressure apparatus.

About 250mg of homogenous powder of starting material is encapsulated into gold capsule of height 4.5mm and kept in a container made of NaCl+20 wt.% ZrO_2 sleeve and disks. This container is enclosed by graphite (acts as heater) sleeve and disk. This enclosed graphite sleeve with Mo plate and stainless steel surrounding the pyrophyllite disk on either side is placed into the solid cubic pyrophyllite, which acts as transmitting medium and gasket. Overall configuration of the sample cell is shown in the Fig.2.1 in chapter 2. This complete sample cell assembly is placed at the base of the bottom wedge shaped anvil. The remaining anvils are placed and leveled around the sample cell such a way that there should be an equal gap between the anvils. After leveling the anvils the synthesis chamber (cubic void formed by the cubic anvil apparatus) is enclosed by placing top anvil on the sample cell. The whole arrangement is moved under the base of the hydraulic press. The sample cell is pressurized by applying 300 tons load (~ 4.5 *GPa* pressure) and heated to1000°C by supplying power~780 W. The reaction temperature is maintained for 1 hour and sample is quenched under pressure 4.5*GPa*. The pressure is then decreased and finally, the sample is taken out at ambient pressure.

3.3.2. Characterization

The phase purity is confirmed by collecting X-Ray diffraction in PANalytical Empyrean alpha-1 X-ray diffractometer where the sample is subjected to Cu Kα-1 radiation (λ=1.5406 Å) in the range of Bragg angle ($10^o \leq 2\theta \leq 120^o$) under θ -2 θ scan. XRD data has been analyzed and crystal structure is refined using Full-Prof suite software by Rietveld refinement [16-17].

3.3.3. Magnetic Measurements

Low temperature DC magnetic measurements were carried out in SQUID VSM (Quantum Design, USA). Temperature dependent FC (Field Cooled) and ZFC (Zero Field Cooled) magnetization data is collected at 1000 Oe in the temperature range of 2 K to 390 K in vibrating sample mode. M *vs.* H data was collected at 2 K and 300 K in magnetic field range of ±60 kOe. High temperature DC magnetization measurements were carried out using a vibrating sample magnetometer(VSM) in Physical Property Measurement System (PPMS) under Zero-Field-Cooled (ZFC) and Field-Cooled (FC) conditions in 300 to 800 K temperature range in the presence of 1000 Oe magnetic field. Low temperature AC magnetization measurements were carried out in Physical Property Measurement System (PPMS, Quantum Design) in temperature range of 5-300 K.

3.4. Results and Discussions

3.4.1. Crystal Structure Analysis

The powder X-ray diffraction patterns of $GaFeO_3$ and $Ga_{0.5}Al_{0.5}FeO_3$ samples revealed that both oxides crystallizing in corundum type (centro symmetric) structure with *R-3c* space group. The refinement made using model *R-3c* space group gave considerable fitting with χ^2 value 2.33% for $GaFeO_3$ and 1.35% $Ga_{0.5}Al_{0.5}FeO_3$. The lattice parameters of are, a = 5.0213 Å, b = 5.0213 Å, c = 13.5949 Å, and a = 4.9689(3) Å, b = 4.9689(3) Å, c = 13.4789(9) Å for $GaFeO_3$ and for $Ga_{0.5}Al_{0.5}FeO_3$, respectively. Rietveld refined XRD pattern of high pressure synthesized $GaFeO_3$ and $Ga_{0.5}Al_{0.5}FeO_3$ is shown in the Fig.3.1. (a) and (b) respectively. Also, presence of center of symmetry in $GaFeO_3$ is confirmed by Second Harmonic Generation

experiment carried out in university of Houston, USA. In this experiment, a laser light of 1064 nm wavelength was used and no green light (532 *nm*) is observed through the sample indicating the presence of center of symmetry in the crystal.

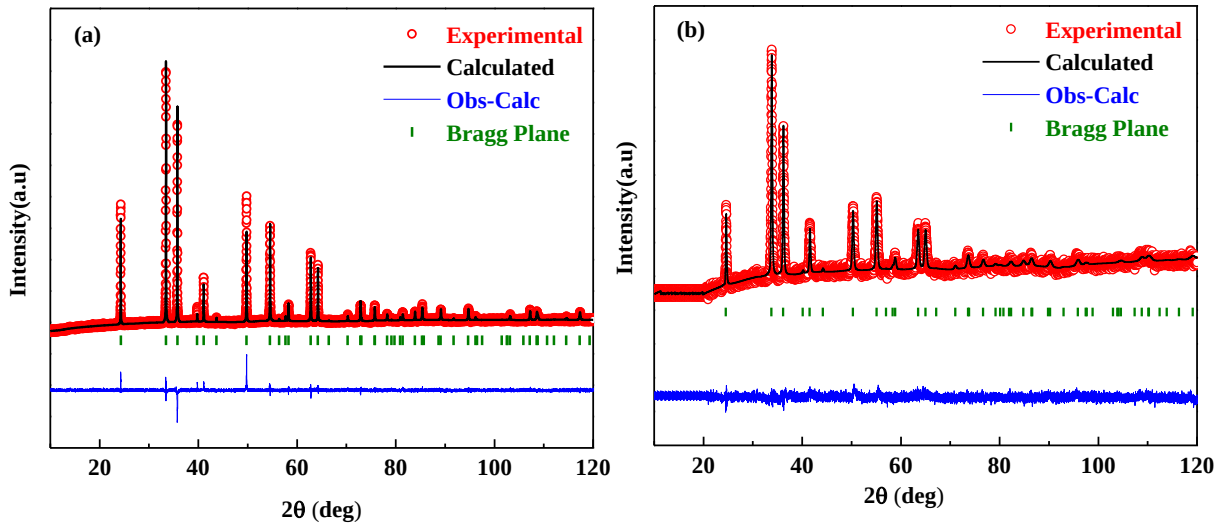

Fig.3.1. Rietveld refined X-ray diffraction pattern of (a) $GaFeO_3$ and (b) $Ga_{0.5}Al_{0.5}FeO_3$

During Rietveld refinement, the occupancy of oxygen is kept fixed to value 1.0 and for cations the occupancy calculated by the formula,

$$\boldsymbol{occupancy = \frac{chemical\ occupancy\ X\ site\ occupancy}{occupancy\ of\ the\ general\ site}}$$

The refined lattice parameters, atomic co-ordinates and thermal parameters of $GaFeO_3$ and $Ga_{0.5}Al_{0.5}FeO_3$ are given in the Table 3.1 and 3.3, respectively and bond length details are given in the Table 3.2 and 3.4, respectively.

Table 3.1: Atomic coordinates of $GaFeO_3$

Space group : R-3c (trigonal), a = 5.0213 Å, b = 5.0213 Å, c = 13.5949 $\alpha = 90^o$, $\beta = 90^o$ and $\gamma = 120^o$					
Atoms	***x/a***	***y/b***	***z/c***	**B_{iso}**	**Occ.**
Ga	0.0000	0.0000	0.1451(6)	0.55(9)	0.16(7)
Fe	0.0000	0.0000	0.1451(6)	0.55(9)	0.16(7)
O	0.2910(4)	0.0000	0.2500	1.000	0.500
$\chi^2 = 2.33\%$					

Table 3.2: Bond lengths of $GaFeO_3$

Site	**Bond**	**Bond length (Å)**
Fe/Ga	Fe/Ga – Ga/$Fe_{(1)}$	2.850(61)
	Fe/Ga – Ga/$Fe_{(2)}$	2.957(42)
	Fe/Ga – $O_{(1)}$	2.041(21)
	Fe/Ga – $O_{(2)}$	2.041(20)
	Fe/Ga – $O_{(3)}$	1.977(30)
	Fe/Ga – $O_{(4)}$	1.977(11)

Subscripts (1) to (4) used to indicate equivalent oxygen and cations in the polyhedra.

Table 3.3: Atomic coordinates of $Ga_{0.5}Al_{0.5}FeO_3$

Space group : R-3c (trigonal), a = 4.9689(3) Å, b = 4.9689(3) Å, c = 13.4789(9) Å $\alpha = 90^o$, $\beta = 90^o$ and $\gamma = 120^o$					
Atoms	***x/a***	***y/b***	***z/c***	**B_{iso}**	**Occ.**
Ga	0.0000	0.0000	0.1446(8)	0.61(4)	0.16(7)
Al	0.0000	0.0000	0.1446(8)	0.61(4)	0.16(7)
Fe	0.0000	0.0000	0.1446(8)	0.61(4)	0.33(3)
O	0.3093(5)	0.0000	0.2500	1.000	1.000
$\chi^2 = 1.35\%$					

Table 3.4: Bond lengths of $Ga_{0.5}Al_{0.5}FeO_3$

Site	**Bond**	**Bond length (Å)**
Ga/Al/Fe	Ga/Al/Fe – Ga/Al/Fe $_{(1)}$	2.839(21)
	Ga/Al/Fe – Ga/Al/Fe $_{(2)}$	2.929(43)
	Ga/Al/Fe – $O_{(1)}$	2.092(21)
	Ga/Al/Fe – $O_{(2)}$	1.908(20)
	Ga/Al/Fe – $O_{(3)}$	1.9077(13)
	Ga/Al/Fe – $O_{(4)}$	1.9077(11)

Subscripts (1) to (4) used to indicate equivalent oxygen and cations in the polyhedra.

The volume of the unit cell of $GaFeO_3$ in *R-3c* phase found to be 296.8(5) $Å^3$ while the insertion of 50% of Al in the place of Ga reduced the volume of the unit cell to 288.2(1) $Å^3$ in the same phase.

The crystal structures of both the oxides are visualized using Diamond-crystal and molecular structure visualization software and shown in the Fig.3.2.

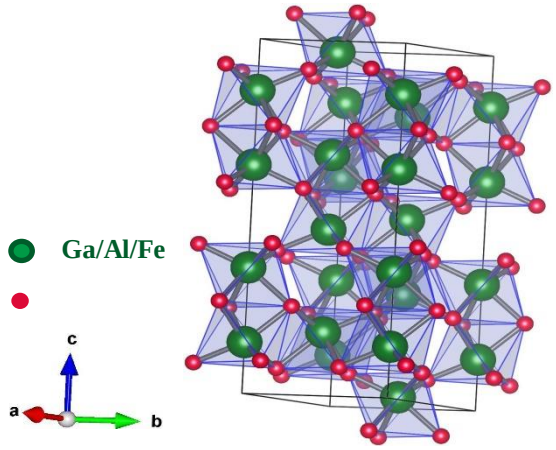

Fig.3.2. Crystal structure of $GaFeO_3$/ $Ga_{0.5}Al_{0.5}FeO_3$

The crystal structure of $GaFeO_3$ and $Ga_{0.5}Al_{0.5}FeO_3$ consists of hexagonal close packed array of oxygen anions surrounding the Al^{3+}, Fe^{3+} or Ga^{3+} cations forming octahedron as shown in the Fig.3.2. These octahedra are sharing faces and edges with each other. The cations occupy 2/3 of the total available octahedral holes in the unit cell. Because of same oxidation state of cations, cationic disorder is observed at the octahedral site. Each cation is coordinated to six oxygen ions form AlO_6/FeO_6/GaO_6 octahedra whereas oxygen is coordinated to four cations. There are total 30 atoms per unit cell consisting of six formula units in the unit cell which are in agreement with other corundum type structure [4].

3.4.2. Magnetic Properties

Temperature dependence of field cooled (FC) and zero-field cooled magnetization curve of $GaFeO_3$ and $Ga_{0.5}Al_{0.5}FeO_3$ under an applied DC field 1000 Oe is shown in the Fig.3.3 and Fig.3.4 (a), (b). From DC magnetic measurement, two anomalies in magnetization are observed in both the oxides. In case of $GaFeO_3$, first anomaly is observed at low temperature T^*~ 45 K and second at high temperature T_N ~ 450 K whereas in case of $Ga_{0.5}Al_{0.5}FeO_3$ first anomaly is observed at low temperature T^*~ 43 K and second at high temperature T_N ~ 650 K. The anomaly observed at 450 K in $GaFeO_3$ and at 650 K in $Ga_{0.5}Al_{0.5}FeO_3$ corresponds to long range antiferromagnetic ordering of Fe^{3+} ions. It should be noted that the T_N of $Ga_{0.5}Al_{0.5}FeO_3$ is much higher than that of $GaFeO_3$. This behavior is unexpected because the structure remains the same with Al^{3+} substitution. Since the T_N of $AlFeO_3$ is not known, we will not be able to comment on this behavior and it requires further investigation. The hysteresis shown in the inset of Fig.3.3 and 3.4(a) and small magnetization value of FC curves at lowest temperature in Fig.3.3 and 3.4(a) indicating the presence of canting of Fe^{3+} spins at room temperature.

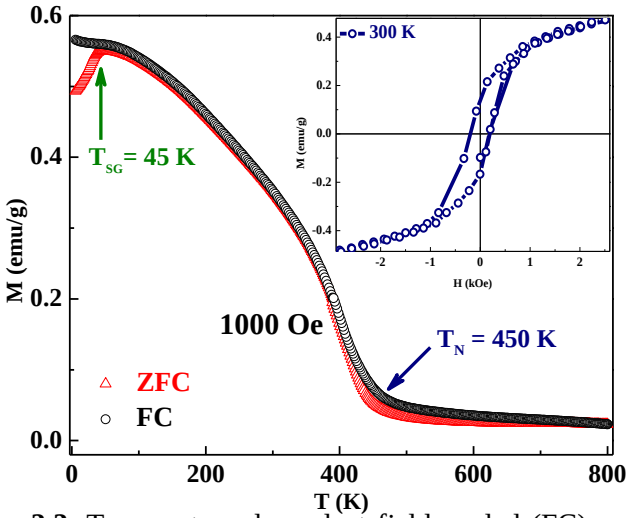

Fig. 3.3. Temperature dependent field cooled (FC) and zero field cooled (ZFC) magnetization under applied field of 1000Oe of $GaFeO_3$. M vs. H data at 300 K is shown in the inset.

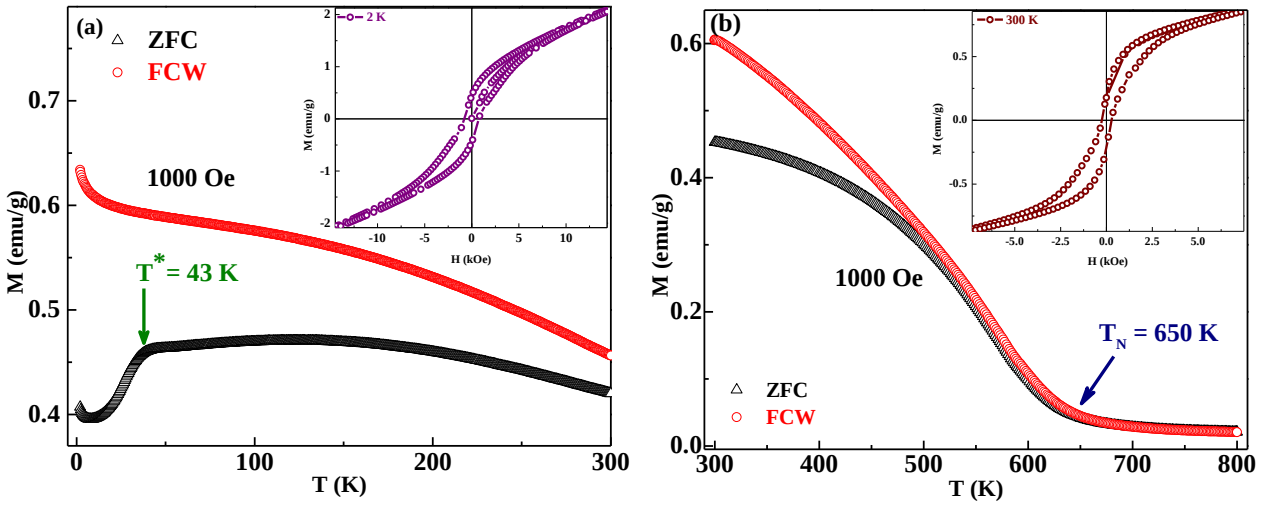

Fig. 3.4. Temperature dependent field cooled (FC) and zero field cooled magnetization (ZFC) under applied field of 1000 Oe of $Ga_{0.5}Al_{0.5}FeO_3$ in (a) low temperature region (2-300 K) with inset of M vs. H data at 2 K (b) high temperature region (300-800 K) with the inset of M vs. H data at 300 K

Let us first focus on the behavior of FC and ZFC curves at low temperatures in $GaFeO_3$. It can be seen that there is a peak in ZFC curve at T*~45 K, below which there is an irreversibility between the ZFC and FC curves. On the other hand, the irreversibility begins at high temperature (~ 500 K) in $Ga_{0.5}Al_{0.5}FeO_3$. However, a similar low temperature anomaly exists (T*~ 43 K) in $Ga_{0.5}Al_{0.5}FeO_3$. The bifurcation of FC and ZFC curves may indicate a spin glass state. To understand this behavior, temperature dependent AC susceptibility measurements have been carried out in both the samples in the temperature, 2-300 K, as shown in the Fig.3.5 and 3.6, respectively.

In AC magnetic susceptibility measurements, on increasing the frequency of the applied ac magnetic field, the shift in freezing temperature has been observed which is a characteristic behavior of spin glass systems. On increasing the frequency of the applied field, the intensity of real component of ac susceptibility (χ') decreases whereas intensity of imaginary component of ac susceptibility (χ'') increases. The shift in freezing temperature is observed at

two different temperature regions for $GaFeO_3$ (Fig 3.5(b)). The shift in low temperature region around 60-90 K, as shown in Fig 3.5(b), corresponds to spin glass freezing temperature T*~45 K. But the origin of the shift in the high temperature region around 140-160 K is unknown as there is no corresponding anomaly in dc magnetization. To understand the occurrence of shift in this region further temperature dependent ac susceptibility under dc field has to be done.

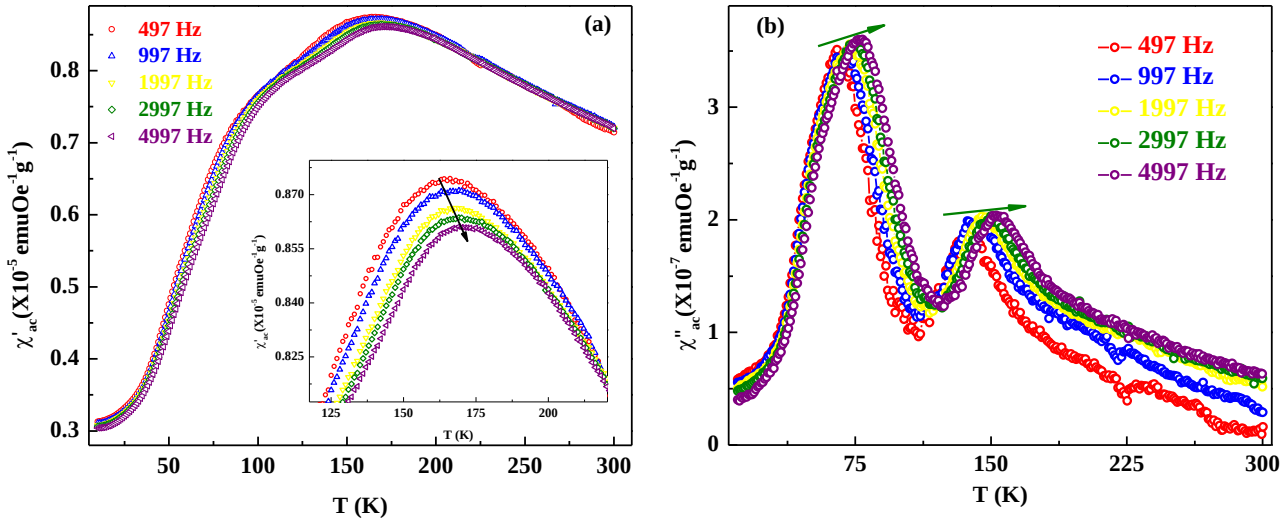

Fig.3.5. Temperature dependent (a) real part of ac susceptibility and (b) imaginary part of ac susceptibility with different frequencies of $GaFeO_3$. Shift of T_f is shown in the inset of (a).

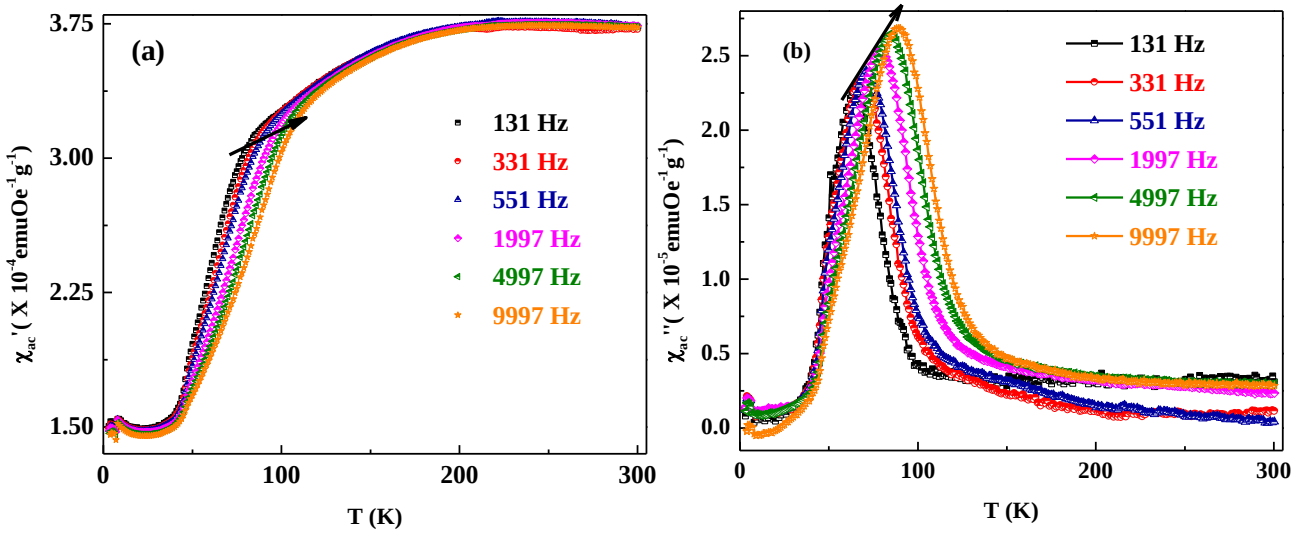

Fig.3.6. Temperature dependent (a) real part of ac susceptibility and (b) imaginary part of ac susceptibility with different frequencies of $Ga_{0.5}Al_{0.5}FeO_3$ with the arrow showing shift of T_f.

In the case of $Ga_{0.5}Al_{0.5}FeO_3$, the ac magnetization measurements carried out for different frequencies resulted in shift of peaks as shown in the Fig 3.6 which corresponds to $T^* \sim$ 43 K observed in DC magnetization measurements (Fig.3.4(a)). It is to be noted that we do not see the high temperature anomaly in this compound. To understand the relaxation behavior of $GaFeO_3$ and $Ga_{0.5}Al_{0.5}FeO_3$, ac susceptibility data is further analyzed using the equation describing critical relaxation behavior of glassy systems [6-8],

$$\frac{\tau}{\tau_o} = \left(\frac{T_f - T_{sg}}{T_{sg}}\right)^{-zv} \text{----------} \quad (1)$$

where τ is the relaxation time for the excitation frequency f, τ_o is the shortest relaxation time to flip the spin, T_{sg} is the spin freezing temperature for $f = 0$ Hz and zv is dynamic critical exponent. Based on this equation, $log_{10}(f)$ vs $log_{10}[(T_f - T_{sg})/T_{sg}]$ is plotted for different frequencies shown in the Fig.3.7(a) for $GaFeO_3$ and (b) for $Ga_{0.5}Al_{0.5}FeO_3$. The plots are fitted using eq.(1). The values zv and τ_o obtained from the above fit are 6.68 and 10^{-7}, respectively for $GaFeO_3$. For $Ga_{0.5}Al_{0.5}FeO_3$, zv value is found to be 9.8 and τ_o is 10^{-7}. Generally, for spin glass system zv varies in the range of 4-12 [9-10] and specifically for cluster spin glasses, τ_o varies in the range of 10^{-7}-10^{-10}[9-10]. Since both these oxides are showing these values in the above range, these are considered to be a cluster spin glass systems. Further, to confirm the cluster spin glass behavior, ac susceptibility data is analyzed using Vogel-Fulcher law [6, 8] which is commonly used estimate the activation energy by the expression,

$$\omega = \omega_o \, exp\left[\frac{-E_a}{k_B\,(T_f - T_o)}\right] \text{----------} \quad (2)$$

where ω is the excitation frequency, ω_o is the frequency corresponding to relaxation time τ_o as $\omega_o = 1/\tau_o$, k_B is Boltzmann constant, E_a is the activation energy required to access different metastable states of spin glass system, T_f is the temperature peak corresponding to frequency f and T_o is the spin freezing temperature.

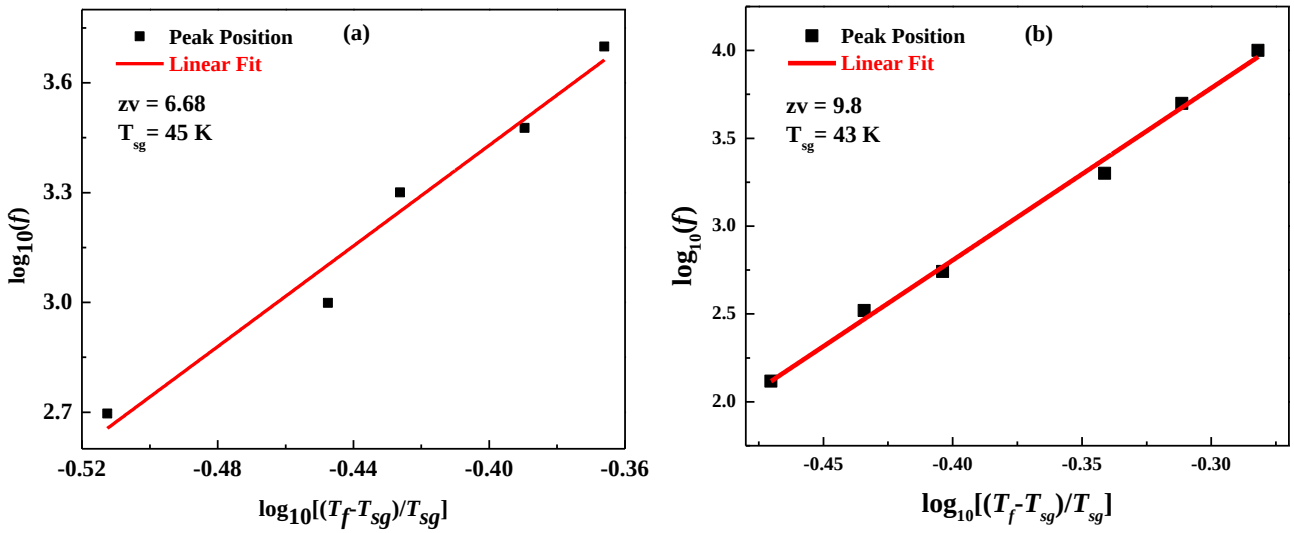

Fig.3.7. Plot of $log_{10}(f)$ vs $log_{10}[(T_f - T_{sg})/T_{sg}]$ for (a)$GaFeO_3$ and (b) $Ga_{0.5}Al_{0.5}FeO_3$ with solid red line representing good fit to the equation (1).

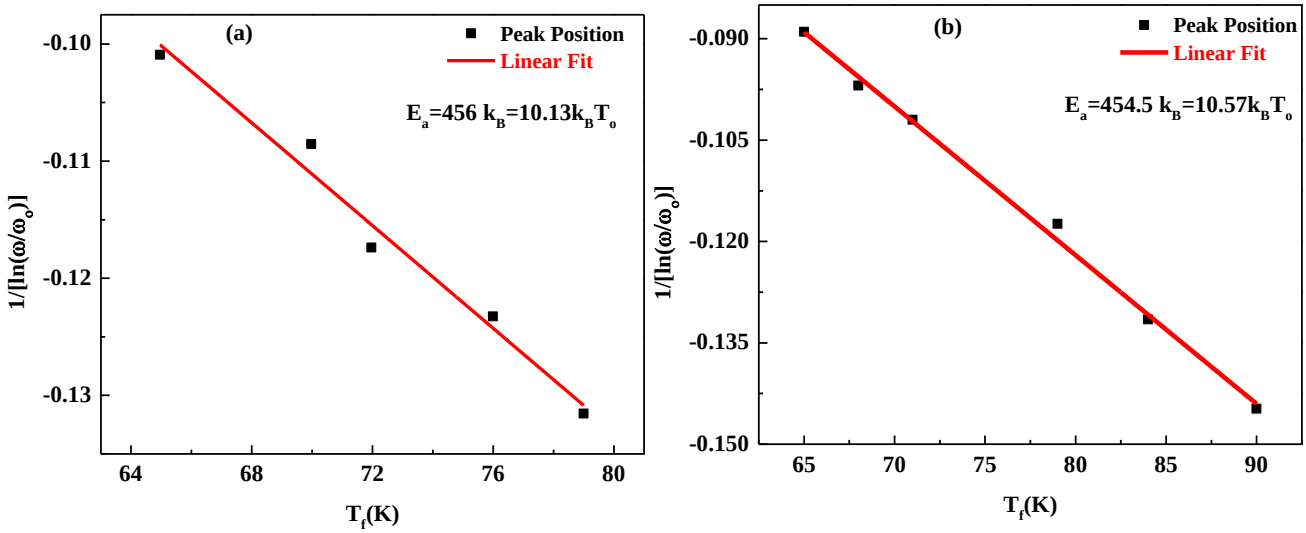

Fig.3.8. Plot of $1/ln(\omega/\omega_o)$ vs. T_f for (a)$GaFeO_3$ and (b) $Ga_{0.5}Al_{0.5}FeO_3$ with the solid red line representing good fit to the equation (2).

Considering $\omega_o = 10^7$ Hz from previous analysis, using Vogel Fulcher law, $1/ln(\omega/\omega_o)$ is plotted against T_f and fitted linearly which has given rise to value of E_a= 10.13 k_BT_o for $GaFeO_3$ and 10.57 k_BT_o for $Ga_{0.5}Al_{0.5}FeO_3$ as shown in the Fig 3.8(a) and (b) respectively. Generally, for canonical spin glass system like CuMn [11] (Mn~ 3.3-8 at.%), E_a is $2k_BT_o$ and for geometrically frustrated spin glass like $CaBaFe_4O_7$[12], E_a~1.25 k_BT_o. In contrast to these systems, cluster spin glasses show high values of E_a. $CaBa_{4-x}Li_xO_7$ (x=0.4) [12] being cluster spin glass have E_a~12k_BT_o. Hence the values of E_a obtained for $GaFeO_3$ and $Ga_{0.5}Al_{0.5}FeO_3$ indicating a cluster spin glass behavior.

The existence of such cluster spin glass state at low temperature is majorly due to the geometrical frustration owing to the presence of cation site disorder in octahedral site where Fe^{3+} moments are interacting antiferromagnetically with each other.

3.5. Decomposition of $AlFeO_3$ under high pressure and high temperature

$AlFeO_3$ in orthorhombic phase ($Pna2_1$) is synthesized by sol gel auto combustion method [13]. $Al(NO_3)_3.9H_2O$ and $Fe(NO_3)_3.9H_2O$ in appropriate stoichiometry is dissolved in water and citric acid of about twice the moles of metal nitrates is dissolved and heated at 80°C on the heating mantle with constant stirring to form gel. Thus formed gel is heated in oven at 200°C for 12 hours to form porous mass which is then annealed in oxygen at 600°C to remove carbon impurities. Further, $AlFeO_3$ is obtained by heating the compound at 1350°C with repeated grinding. XRD analysis confirmed the phase of thus obtained $AlFeO_3$ as orthorhombic ($Pna2_1$). About 250 mg of $AlFeO_3$ is used a starting material and high pressure reactions are done at 700°C, 750°C, 800°C and 1000°C by applying pressure 4.5*GPa* (~300 tons load) with high temperature maintained for 1 hour. After the reaction the phase of the sample is analyzed by

Bruker D8 Advance X-ray diffractometer. XRD patterns obtained for $AlFeO_3$ synthesized at different high temperatures and constant high pressure are given in the Fig. 3.9.

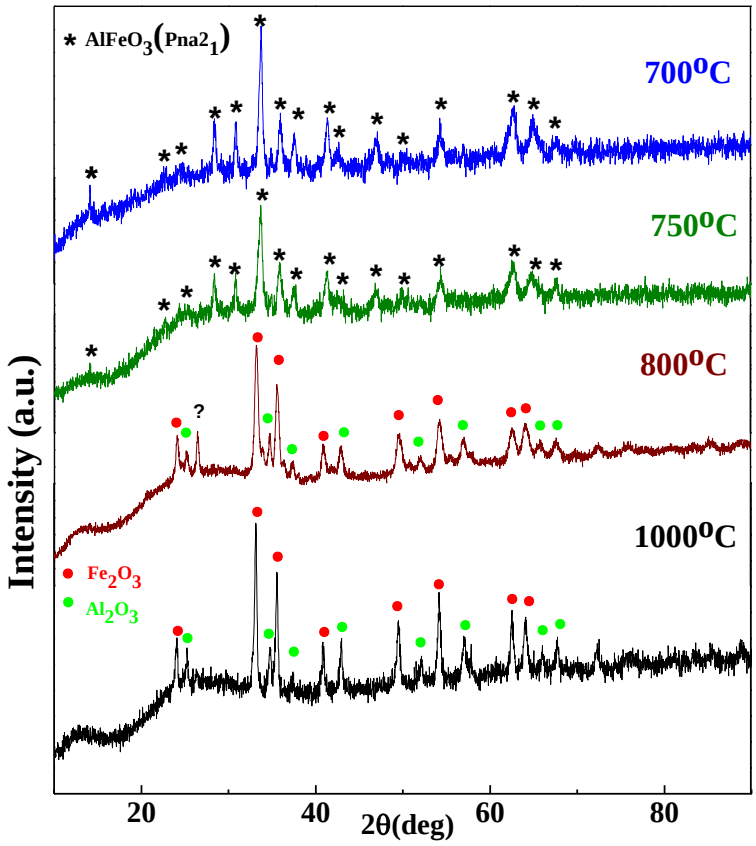

Fig.3.9. XRD pattern of $AlFeO_3$ synthesized at 4.5*GPa* at different temperatures 700°C, 750°C, 800°C and 1000°C .

From Fig.3.9, it can be observed that the phase of $AlFeO_3$ heated at 700°C and & 750°C under 4.5*GPa* pressure remained in $Pna2_1$ phase. But the samples heated at 800°C under same pressure decomposed to constituent oxides Al_2O_3(*R-3c*) and Fe_2O_3 (*R-3c*) with an unknown peak indicated by symbol '?' at 800°C. Further, high pressure synthesis carried out at temperature 1000°C resulted in complete decomposition of $AlFeO_3$ in the constituent Al_2O_3 and Fe_2O_3 in *R-3c* phases. Decomposition of any oxide under high pressure is rarely found. Recently,

decomposition of $La_2Hf_2O_7$ beyond pressure ~ 18 *GPa* into its constituent oxides La_2O_3 and HfO_2 is reported [14].

$AlFeO_3$ in orthorhombic (*Pna2₁*) phase using Al_2O_3 and Fe_2O_3 (both in *R-3c*) by solid state method is difficult to synthesize. This may be because of difference in the ionic radii of Al^{3+}~ 0.53 Å and Fe^{3+} ~ 0.64 Å [18-19]. Hence to stabilize $AlFeO_3$ in orthorhombic phase generally wet chemistry methods are employed which helps compound in attaining metastable phase. Application of high pressure and temperature on such metastable phase results in structural instability and may give rise to decomposition or phase transition. The phase transition of $AlFeO_3$ of orthorhombic (*Pna2₁*) phase to rhombohedral (*R-3c*) phase is reported to occur by applying high pressure ~ 72 *GPa* and temperature 1800 K with the $AlFeO_3$ in *Pna2₁* phase as starting material [13]. But the decomposition of $AlFeO_3$ to constituent oxides for an intermediate pressure observed in present study can be explained by Pauling's third rule [15]. According to this rule, in coordinated structure, presence of edge sharing polyhedron and specially face sharing polyhedron decreases the stability of polyhedron and if the radius ratio is in the lower bound decreases the stability further. This is because the distance between the cations in the polyhedra that share corners is considered as 1, that sharing edges decreases the distance to 0.58, and sharing of faces decreases the distance to 0.38. Hence the electrostatic repulsion between the cations increases making the polyhedral unstable. In case of corundum (*R-3c)* type structure, the oxygen anions form an octahedron with the cation at the octahedral hole. These octahedral share edges as well as faces. Hence repulsive force between the cations is more. The structure remains stable only when the repulsive force between the cations and attractive force between anions and cations balance each other. In case of $AlFeO_3$, in orthorhombic phase there are corner sharing tetrahedra and edge sharing octahedral are present. There is a possibility that

application of very high pressures and high temperature may overcome the repulsive forces and can stabilize the corundum type *(R-3c)* structure in $AlFeO_3$. This seems to be achieved with a pressure of ~72 *GPa* and a temperature 1800 K [13]. But application of relatively low pressure (4.5*GPa*) and temperature (1000°C) does not seem to overcome the repulsive forces.

3.6. Conclusions

X-ray diffraction and second harmonic generation experiments have done to analyse the structure of $GaFeO_3$ and $Ga_{0.5}Al_{0.5}FeO_3$ which were prepared under high pressure (4.5 *GPa*) and high temperature (1000 °C). The magnetic studies on both the oxides revealed the presence of long range antiferromagnetic order above room temperature with slight spin canting. Presence cluster spin glass state at low temperature is evidenced from the results of ac susceptibility measurements. Cation disorder at octahedral site is found to be main reason for origin of cluster spin glass behavior at low temperature. Also, instability of $AlFeO_3$ and its decomposition into its constituent oxides Al_2O_3 (*R-3c*) and Fe_2O_3(*R-3c*) upon application of high pressure and high temperature is studied.

3.7. Bibliography

1. Rana Saha et al., *Solid State Communications*, **152** (2012)

2. R.B. Frankel, N.A. Blum, S. Foner, A.J. Freeman, M. Schieber, *Phys. Rev. Lett.* **15** (1965) 958.

3. Rana Saha et al.,*Inorg. Chem.*, **50**, 9527–9532(2011)

4. Xiao-Gang Wang, Anne Chaka, and Matthias Scheffler, *Phys. Rev. Lett.* **84**, 3650 (2000)

5. Somdutta Mukherjee, Ashish Garg and Rajeev Gupta, *Appl. Phys. Lett.* **100**, 112904 (2012)

6. J. A. Mydosh, Spin Glasses: An Experimental Introduction, Vol. 125 (Taylor & Francis, London, 1993)

7. P. C. Hohenberg and B. I. Halperin, *Rev. Mod. Phys*. **49**, 435 (1977).

8. K. Binder and A. P. Young, *Rev. Mod. Phys*. **58**, 801 (1986).

9. J. Lago, S. J. Blundell, A. Eguia, M. Jansen, and T. Rojo, *Phys. Rev. B* **86**, 064412 (2012)

10. A. Malinowski, V. L. Bezusyy, R. Minikayev, P. Dziawa, Y. Syryanyy, and M. Sawicki, *Phys. Rev. B* **84**, 024409 (2011)

11. C. A. M. Mulder, A. J. van Duyneveldt, and J. A. Mydosh, *Phys. Rev. B* **23**, 1384 (1981)

12. 9K. Vijayanandhini, C. Simon, V. Pralong, V. Caignaert, and B. Raveau, *Phys. Rev. B* **79**, 224407 (2009)

13. Takaya Nagai et al, *J. Phys. Chem. B*, **109**,39 (2005)

14. Nandini Garg, A.K. Tyagi et al, *Phys. Rev. B* **77**, 214105 (2008)

15. Pauling, Linus, *J. Am. Chem. Soc*. **51** (4): 1010–1026(1929)

16. Rietveld, M., H.; Acta Crystallographica. 1967, 22, 15.

17. Rietveld, M., H.; Journal of Applied Crystallography.1969, 2, 65.

18. Shannon, RD, *Acta crystallographica section A: crystal physics, diffraction, theoretical and general crystallography* 32.5 (1976): 751-767.

19. Shannon, RD T., and C. Tfc Prewitt. *Acta Crystallographica Section B: Structural Crystallography and Crystal Chemistry* 25.5 (1969): 925-946.

Chapter 4

Synthesis and Magnetic Properties of $ACrO_3$ (A=Al, Ga) Oxides

Summary

Ternary chromium oxides $AlCrO_3$ and $GaCrO_3$ are synthesized and found to be crystallizing in corundum (*R-3c*) structure. $AlCrO_3$ forms under ambient pressure and high temperature but $GaCrO_3$ requires high pressure~ 4.5 *GPa* and high temperature ~ 1000°C. Both oxides $AlCrO_3$ and $GaCrO_3$ show long range antiferromagnetic ordering at Neel temperatures T_N ~115 K and T_N ~ 95 K, respectively. The presence of small Cr-O bond in $AlCrO_3$ may be responsible for high Neel temperature in $AlCrO_3$ than that of $GaCrO_3$. The substitution of Fe in the place of Cr in $AlCrO_3$ gives rise to $AlCr_{0.5}Fe_{0.5}O_3$ crystallizing in corundum (*R-3c*) structure and induces the weak ferromagnetism at temperature T_N~ 270 K.

4.1. Introduction

$ACrO_3$ oxides found to be crystallize in corundum (*R-3c*) structure while most of the $ACrO_3$ compounds with bigger A-cations such as Sc, In and rare earths (R=Y, Lu) known to crystallize in perovskite structure with orthorhombic symmetry [1]. Synthesis of $ScCrO_3$ and $InCrO_3$ requires high pressure and temperature [2-3]. Another ternary oxide $BiCrO_3$, synthesized under high pressure 35-55 *kbar* and high temperature 700-800°C crystallizes in perovskite structure with monoclinic crystal symmetry [4-5]. Oxides such as $FeCrO_3$ [7] and $CrVO_3$ [6] can

be synthesized under ambient pressure and high temperature which crystallize in corundum *R-3c* phase whereas some oxides like $MnCrO_3$ [8] and $NiCrO_3$ [9] requires high pressure that crystallize in the ilmenite corundum type structure.

Present work mainly focuses on the synthesis of corundum type $AlCrO_3$ and $GaCrO_3$ in ambient and high pressure and comparative study of their magnetic properties.

4.2. Scope of the investigation

Present investigations on corundum type $AlCrO_3$ and $GaCrO_3$ helps to understand the magnetic behavior of $ACrO_3$ compounds with two different A cations. Thus, two more ternary chromium oxides with comparative magnetic properties have been added to the list of other corundum type chromium oxides.

4.3. Experimental Details

4.3.1. Synthesis

$AlCrO_3$ was synthesized by solid state method at ambient pressure and $GaCrO_3$ was synthesized by heating the mixture of constituent oxides under high pressure. While synthesizing $AlCrO_3$, the stoichiometric amounts of constituent oxides α-Al_2O_3 (99.9%) and Cr_2O_3 (99.9%) in powder form are mixed and mixed thoroughly using mortar and pestle and heated at 1400°C at the rate of 5°C/min with repeated grinding, pelletizing and heating. For the synthesis of $GaCrO_3$, the component oxides β-Ga_2O_3 (99.9%) and Cr_2O_3 (99.9%) in powder form are thoroughly mixed. This mixed powder was used for high pressure synthesis of $GaCrO_3$. This reaction was carried out under high pressure using a wedge-type cubic-anvil high pressure apparatus.

About 230 mg of homogenous powder of sample is encapsulated into gold capsule of height 4.5 mm and covered by closed hollow cylindrical container made of NaCl+20 wt.% ZrO_2 sleeve and disks. This container is further enclosed with a graphite (acts as heater) sleeve and disk. This enclosed graphite cylinder with Mo plate and stainless steel surrounding the pyrophyllite disk on either side is put into the solid cubic pyrophyllite (acts as pressure transmitting media). Overall design of the sample cell assembly is shown in the Fig. 2.4 in chapter 2. This complete sample cell is placed on the base of the bottom wedge shaped anvil. The remaining anvils are placed properly and leveled around the sample cell (pyrophyllite) such a way that there is equal gap between the anvils. After leveling the anvils properly, the synthesis chamber (enclosed cubic void by anvils) is covered by placing top anvil on the sample cell. The whole arrangement is moved under the bottom of the hydraulic press. The sample cell is pressurized by applying load of 300 tons (~ 4.5 *GPa* pressure) and heated to high temperature 1000°C by supplying a heater power ~ 780 W. The reaction is carried out and temperature is maintained for 1 hour after which the sample was quenched under high pressure *4.5GPa*. The pressure was then decreased at constant rate and finally, at ambient pressure the sample is taken out.

4.3.2. Characterization

The purity of the sample was confirmed by collecting X-Ray Diffraction data in PANalytical Empyrean alpha-1 X-ray diffractometer where the sample was irradiated to Cu Kα-1 radiation (λ=1.5406 Å) in the scan range, $10° \leq 2\theta \leq 120°$ under θ -2 θ. XRD data was analyzed and using Full-Prof Suite software, crystal structure was refined by Rietveld refinement [10-11].

4.3.3. Magnetic Measurements

DC magnetic measurements were done in SQUID VSM (Quantum Design, USA). Temperature dependent Field Cooled (FC) and Zero Field Cooled (ZFC) magnetization measurement is carried out in the presence of field 100 Oe in of 2 K to 390 K temperature range in Vibrating sample mode. M *vs.* H data was collected at 300 K and 2 K in magnetic field range of ±60 kOe.

4.4. Results and Discussion

4.4.1. Crystal Structure Analysis

(a) XRD Results of $AlCrO_3$ and $GaCrO_3$

The powder X-ray diffraction data of $AlCrO_3$ and $GaCrO_3$ samples were analysed and found to be crystallizing in corundum type (centrosymmetric) crystal structure with *R-3c* space group. The refinement made using *R-3c* model gave considerable fitting with χ^2 value 2.17% for $AlCrO_3$ and 2.05% $GaCrO_3$. The lattice parameters of $AlCrO_3$ obtained using refinement are a = 4.87322(7) Å, b = 4.87322(7) Å, c = 13.30850(2) Å and for $GaCrO_3$, a = 4.98236(4) Å, b = 4.98236(4) Å, c = 13.49835(1) Å. Rietveld refined XRD profiles of $AlCrO_3$ and $GaCrO_3$ is shown in the Fig.4.1. (a) and (b), respectively. Also, presence of inversion symmetry (center of symmetry) in $AlCrO_3$ and $GaCrO_3$ is confirmed by Second Harmonic Generation experiment done in university of Houston, USA.

During the refinement the occupancy of oxygen was kept fixed to 0.5. Owing to the presence of cation site disorder, the atomic co-ordinates and B_{iso} values are refined simultaneously.

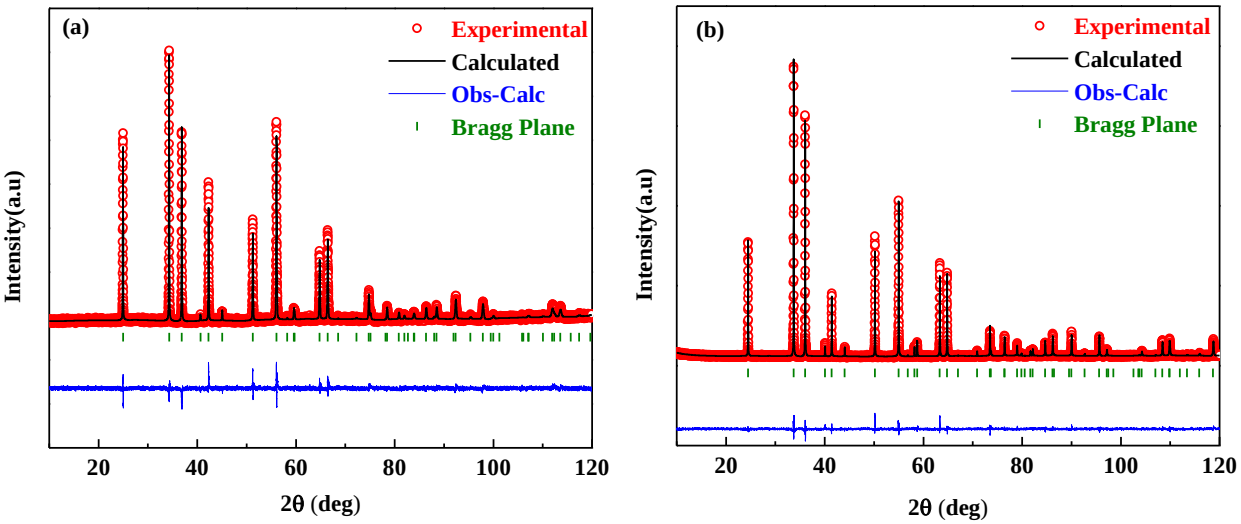

Fig.4.1. Rietveld refined X-ray diffraction profile of (a) $AlCrO_3$ and (b) $GaCrO_3$

The refined lattice parameters, atomic co-ordinates, thermal parameters and occupancy of $AlCrO_3$ and $GaCrO_3$ are given in the Table 4.1 and 4.3, respectively and the details of bond lengths between different atoms are given in the Table 4.2 and 4.4, respectively.

Table 4.1: Atomic coordinates of $AlCrO_3$

Space group : *R-3c* (trigonal), a = 4.87322(7) Å, b = 4.87322(7) Å, c = 13.30850(2) Å α = 90°, β = 90° and γ = 120°					
Atoms	***x/a***	***y/b***	***z/c***	**B_{iso}**	**Occ.**
Al	0.0000	0.0000	0.3491(2)	0.30(2)	0.16(7)
Cr	0.0000	0.0000	0.3491(2)	0.30(2)	0.16(7)
O	0.3100(3)	0.0000	0.2500	1.000	0.50
χ^2 = 2.17%					

Table 4.2: Bond lengths of $AlCrO_3$

Site	Bond	Bond length (Å)
Al/Cr	Al/Cr-Cr/Al $_{(1)}$	2.6383(9)
	Al/Cr-Cr/Al $_{(2)}$	2.8447(6)
	Al/Cr – $O_{(1)}$	2.0056(1)
	Al/Cr – $O_{(2)}$	2.0056(7)
	Al/Cr – $O_{(3)}$	1.9090(7)
	Al/Cr – $O_{(4)}$	1.9090(8)
	Al/Cr – $O_{(5)}$	1.9090(1)

Subscripts (1) to (5) used to indicate equivalent oxygen and cations in the polyhedra.

Table 4.3: Atomic coordinates of $GaCrO_3$

Space group : R-3c (trigonal), a = 4.98236(4) Å, b = 4.98236(4) Å, c = 13.49835(1) Å $\alpha = 90^o$, $\beta = 90^o$ and $\gamma = 120^o$					
Atoms	***x/a***	***y/b***	***z/c***	**B_{iso}**	**Occ.**
Ga	0.0000	0.0000	0.3526(6)	0.087(1)	0.16(7)
Cr	0.0000	0.0000	0.3526(6)	0.087(1)	0.16(7)
O	0.3079(5)	0.0000	0.2500	1.000	0.50
$\chi^2 = 2.05\%$					

Table 4.4: Bond lengths of $GaCrO_3$

Site	Bond	Bond length (Å)
Ga/Cr	Ga/Cr – Ga/Cr $_{(1)}$	2.7715(1)
	Ga/Cr – Ga/Cr $_{(2)}$	2.92350(1)

Ga/Cr	Ga/Cr – $O_{(1)}$	2.0673(19)
	Ga/Cr – $O_{(2)}$	2.0673(10)
	Ga/Cr – $O_{(3)}$	1.9316(10)
	Ga/Cr – $O_{(4)}$	1.9316(13)
	Ga/Cr – $O_{(5)}$	1.932(2)

Subscripts (1) to (5) used to indicate equivalent oxygen and cations in the polyhedra.

From XRD data analysis, the volume of the unit cell of $AlCrO_3$ in R-3c phase found to be 273.7(1) $Å^3$ while that of $GaCrO_3$ is 290.1(8) $Å^3$ phase because of large size of Ga^{3+} ion, 0.62 Å than that of Al^{3+}, 0.53 Å [13-14] .

(a) Neutron Powder Diffraction Results of $AlCrO_3$

In addition to XRD, neutron diffraction analysis was also carried out on $AlCrO_3$ to determine the crystal structure. Rietveld refined neutron diffraction profile for $AlCrO_3$ at 300K is shown in the Fig 4.2.

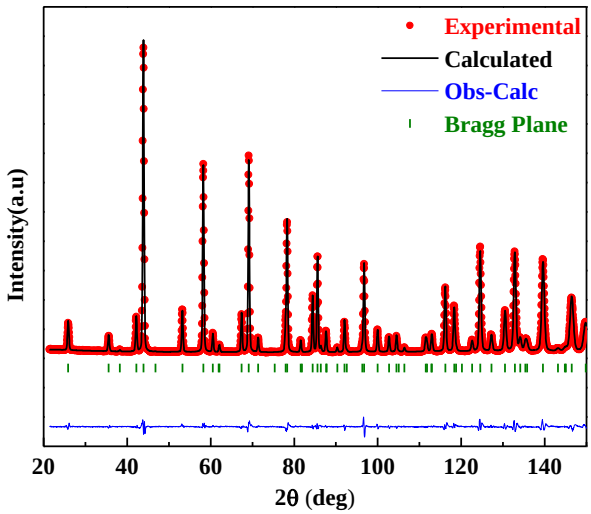

Fig.4.2. Rietveld refined neutron powder diffraction profile of $AlCrO_3$

Rietveld analysis of the neutron diffraction profile confirms the single phase formation of the $AlCrO_3$ crystallizing in the corundum type (*R-3c*) structure. Goodness of the profile fit is found to be 6.61%. The refined lattice parameters, atomic co-ordinates, isotropic thermal parameters and occupancy of $AlCrO_3$ are given in the Table 4.5.and the details of bond lengths between different atoms are given in the Table 4.6.

Table 4.5: Atomic coordinates of $AlCrO_3$

Space group : R-3c (trigonal), a = 4.8675(3) Å, b = 4.8675(3) Å, c = 13.2925(9)Å $\alpha = 90^o$, $\beta = 90^o$ and $\gamma = 120^o$					
Atoms	***x/a***	***y/b***	***z/c***	**B_{iso}**	**Occ.**
Al	0.0000	0.0000	0.3500(8)	0.30(2)	0.16(7)
Cr	0.0000	0.0000	0.3500(8)	0.30(2)	0.16(7)
O	0.3060(8)	0.0000	0.2500	0.336(9)	0.50
$\chi^2 = 6.61\%$, R_{wp} = 7.75 %, R_p = 7.03 %, R_{exp} = 3.01 %, R_{Bragg} = 1.59 %					

Table 4.6: Bond lengths of $AlCrO_3$

Site	**Bond**	**Bond length (Å)**
Al/Cr	Al/Cr-Cr/Al $_{(1)}$	2.6606(1)
	Al/Cr-Cr/Al $_{(2)}$	2.8453(2)
	Al/Cr – $O_{(1)}$	1.9974(6)
	Al/Cr – $O_{(2)}$	1.9102(4)
	Al/Cr – $O_{(3)}$	1.9102(5)

Subscripts (1) to (3) used to indicate equivalent oxygen and cations in the polyhedra.

The refined parameters of $AlCrO_3$ using XRD and NPD are very close but the NPD results are more precise than XRD because using neutron powder diffraction data, the oxygen position and the isotropic thermal parameters of small atom like oxygen can also be refined.

The crystal structure of $AlCrO_3$ and $GaCrO_3$ are visualized using a software namely Diamond-crystal and molecular structure visualization and is shown in the Fig.4.3. Both $AlCrO_3$ and $GaCrO_3$ structures are corundum type and is consists of hexagonal stacking of oxygen anions surrounding the cations Al^{3+}, Cr^{3+} in $AlCrO_3$ and Ga^{3+}, Cr^{3+} cations in $GaCrO_3$ forming octahedron as shown in the Fig.4.3. The cations are situated in the octahedral site coordinated to six oxygen ions and these octahedra are sharing edges and faces with each other.

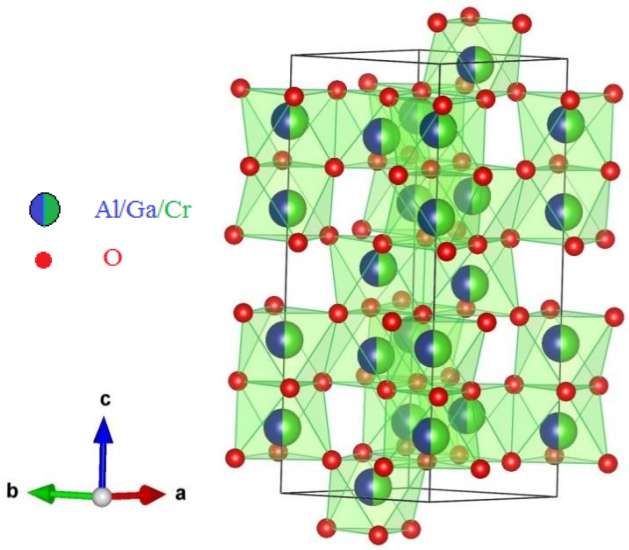

Fig.4.3. Crystal structure of $AlCrO_3$/ $GaCrO_3$

The coordination number of oxygen is four in crystal and is in agreement with other corundum type structure [12]. 2/3 of all available octahedral sites are occupied by cations. Also, cation disorder is observed at octahedral site owing to the presence of cations of same oxidation state. Totally, six formula units are present in each unit cell.

4.4.2. Magnetic Properties

Temperature dependence of FC (field cooled) and ZFC (zero-field cooled) magnetic susceptibility curve of $AlCrO_3$ and $GaCrO_3$ under an applied DC field 100Oe is shown in the Fig.4.4 and Fig.4.5, respectively. From DC magnetic measurement, a magnetic anomaly is found around T_N ~ 115 K for $AlCrO_3$ and T_N ~ 95 K for $GaCrO_3$. The θ_{CW} values calculated by the Curie Weiss fit in paramagnetic region for $AlCrO_3$ and $GaCrO_3$ are -344.6 K and -362.8 K. Such a high negative values of Curie Weiss temperature indicates the presence magnetic frustration because of the disorder of Ga(Al) and Cr ions at the same crystallographic site. Also effective magnetic moment calculated by the Curie Weiss fit for $AlCrO_3$ and $GaCrO_3$ are 3.67μ_B and 4.52 μ_B respectively.

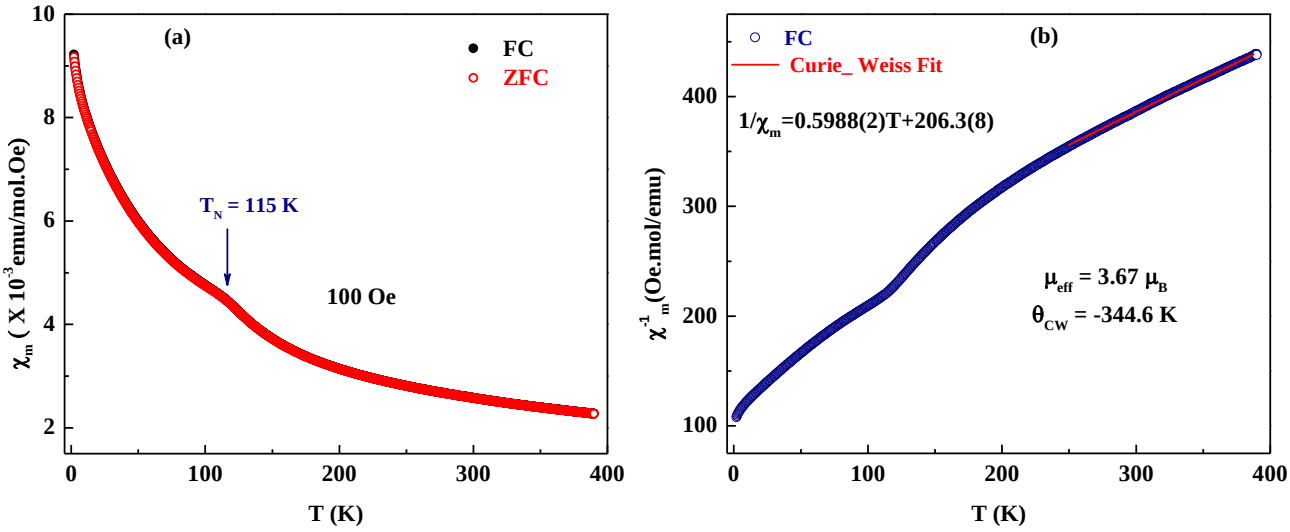

Fig.4.4. (a) Temperature dependent field cooled (FC) and zero field cooled (ZFC) magnetic susceptibility under applied field of 100Oe and (b) Curie Weiss fit on FC inverse magnetic susceptibility of $AlCrO_3$

The spin only magnetic moment calculated for Cr^{3+} ion is 3.87μ_B which is in closely agreement with effective magnetic moment of $AlCrO_3$ and for GaCrO3 it is found to be much higher. From the Table 4.2 and 4.4., it can be observed that the bond length of Cr-O bond is small in case of $AlCrO_3$ than $GaCrO_3$ which results in increased superexchange interaction in $AlCrO_3$ than

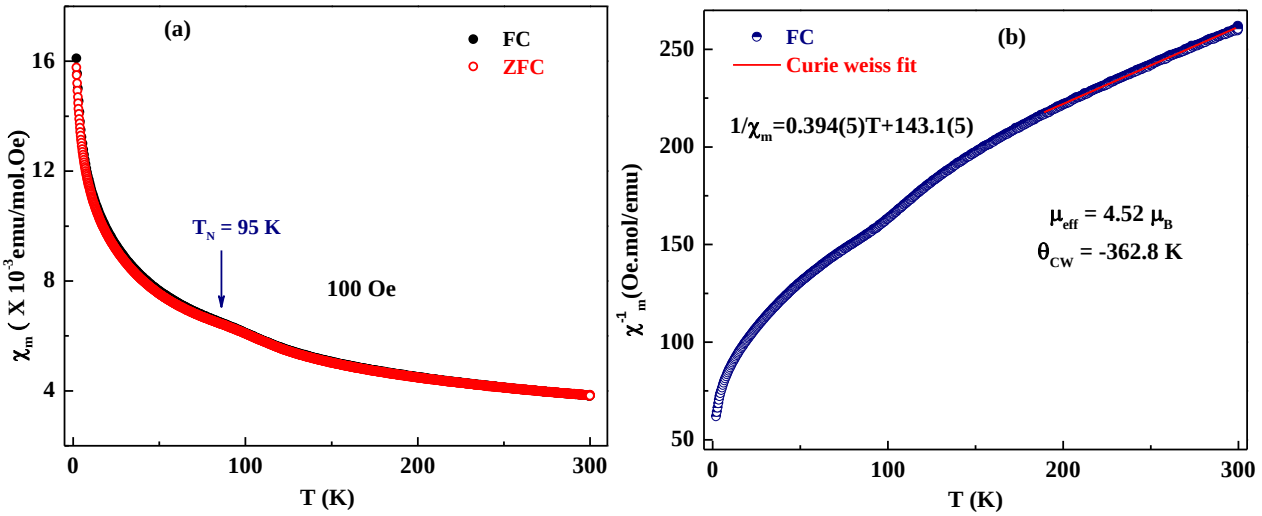

Fig.4.5. (a) Temperature dependent field cooled (FC) and zero field cooled (ZFC) magnetic susceptibility under applied field of 100Oe and (b) Curie Weiss fit on FC inverse magnetic susceptibility of $GaCrO_3$

$GaCrO_3$. Hence exchange energy for $AlCrO_3$ is more than $GaCrO_3$ which could overcome the thermal fluctuations and helps in attaining magnetic ordering at high temperature. So, the Neel temperature is high in case of $AlCrO_3$ than $GaCrO_3$.

4.4.3. Effect of substitution of Fe on magnetic properties of $AlCrO_3$

(a) XRD Results of $AlCr_{0.5}Fe_{0.5}O_3$

The substitution of 50% of Fe in the place of Cr in $AlCrO_3$ is carried out by synthesizing $AlCr_{0.5}Fe_{0.5}O_3$ using solid state method. The crystal structure is analyzed by refining XRD data using Rietveld refinement method and found that $AlCr_{0.5}Fe_{0.5}O_3$ crystallizes in centrosymmetric corundum type (*R-3c*) structure. The end members of $AlCr_{(1-x)}Fe_xO_3$ series are $AlCrO_3$ which crystallize in centrosymmetric corundum structure with trigonal symmetry (R-3c) whereas $AlFeO_3$ synthesized under ambient pressure crystallize in non centrosymmetric orthorhombic ($Pna2_1$) structure. But for x=0.5, it has been found that $AlCr_{0.5}Fe_{0.5}O_3$ adopts $AlCrO_3$ structure rather than that of $AlFeO_3$. It is possible only when free energy formation of

crystal is negative for corundum structure than that of orthorhombic for this compound. The XRD profile of $AlFe_{0.5}Cr_{0.5}O_3$ is shown in the Fig.4.6. Also the lattice parameters and other structural details are given in the table Table 4.7.

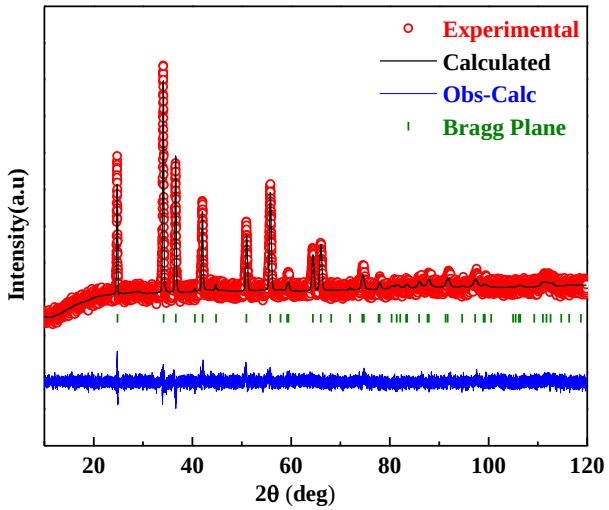

Fig.4.6. Rietveld refined X-ray diffraction profile of (a) $AlCr_{0.5}Fe_{0.5}O_3$

Table 4.7: Atomic coordinates of $AlCr_{0.5}Fe_{0.5}O_3$

Space group : *R-3c* (trigonal), a = 4.9005(3) Å, b = 4.9005(3) Å, c = 13.3509(1) Å $\alpha = 90^o$, $\beta = 90^o$ and $\gamma = 120^o$					
Atoms	***x/a***	***y/b***	***z/c***	**B_{iso}**	**Occ.**
Al	0.0000	0.0000	0.35154(9)	0.97(6)	0.22(2)
Cr	0.0000	0.0000	0.35154(9)	0.97(6)	0.11(1)
Fe	0.0000	0.0000	0.35154(9)	0.97(6)	0.11(1)
O	0.3120(6)	0.0000	0.2500	1.0	0.166(6)
$\chi^2 = 1.30\%$					

(b) Magnetic properties of $AlCr_{0.5}Fe_{0.5}O_3$

Temperature dependence of FC (field cooled) and ZFC (zero-field cooled) magnetization curve of $AlCr_{0.5}Fe_{0.5}O_3$ under an applied DC field 100Oe is shown in the Fig.4.7 (a) and the M vs. H data at 2K is shown in the inset of 4.7(a) at 300 K is shown in 4.7 (b).

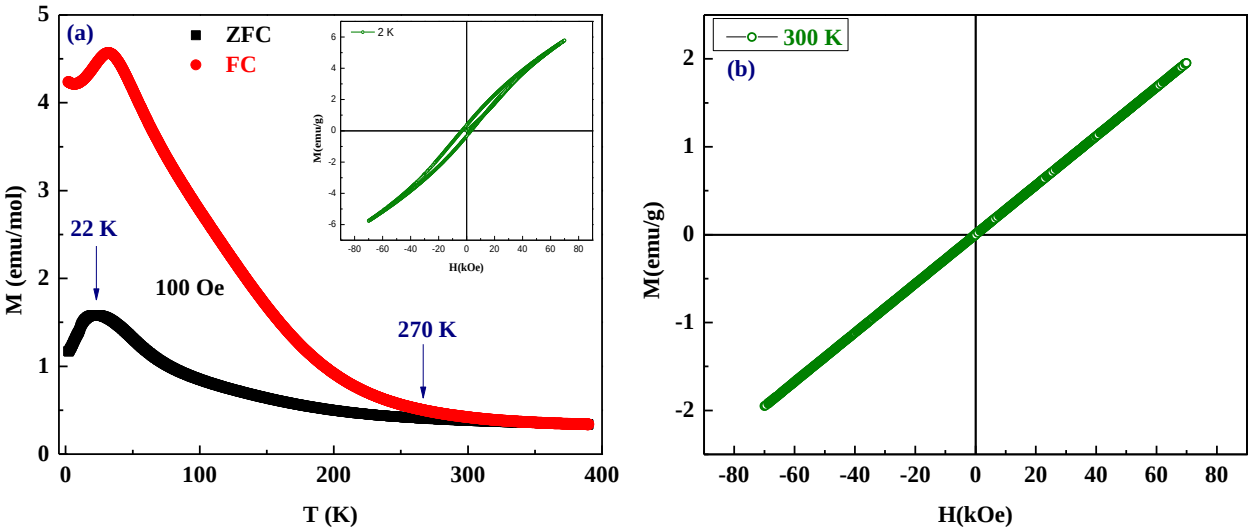

Fig.4.7. (a) Temperature dependent field cooled (FC) and zero field cooled (ZFC) magnetization under applied field of 100Oe with M vs H at 2 K is shown in the inset and (b) M vs H at 300 K of $AlCr_{0.5}Fe_{0.5}O_3$

FromFig.4.7. (a), it is clear that the magnetization value starts increasing below T_N~270 K and the irreversibility between the FC and ZFC curves indicate the presence of weak ferromagnetism below that temperature. M vs. H data at 2 K in the inset of Fig.4.7.(a) also evident for presence of weak ferromagnetism. The origin of weak ferromagnetism by substitution of Fe in $AlCrO_3$ is due to the presence of spin canting. Also, in low temperature region there is a bending of FC and ZFC magnetization curve observed at T~22 K. The bifurcation of FC and ZFC curve observed due to the presence of spin glass state below T~22 K. To confirm such states at low temperature ac susceptibility measurements and other relaxation measurements need to be done.

4.5. Conclusions

X-ray diffraction and Rietveld refinement is done to analyze the structure of $AlCrO_3$ and $GaCrO_3$. Stabilization of corundum structure of $AlCrO_3$ is possible by ambient pressure synthesis but for $GaCrO_3$, high pressure ~ 4.5*GPa* and high temperature 1000°C is required to stabilize its phase in same structure. Presence of long range antiferromagnetic ordering is observed at T_N~115 K and T_N~95 K in $AlCrO_3$ and $GaCrO_3$ oxides. Also, 50% substitution of Fe in place of Cr in $AlCrO_3$ resulted in $AlCr_{0.5}Fe_{0.5}O_3$ crystallizing in corundum (*R-3 c*) structure. Magnetic studies on $AlCr_{0.5}Fe_{0.5}O_3$ revealed that insertion of Fe in the place of Cr in $AlCrO_3$ induces weak ferromagnetism below T_N~270 K.

4.6. Bibliography

1. Belik, Alexei A., and Wei Yi. *Journal of Physics: Condensed Matter* 26.16, 163201(2014).

2. Shannon R D 1967 *Inorg. Chem.* 6 1474

3. Park J H and Parise J B 1997 *Mater. Res. Bull.* 32 1617

4. Niitaka, S., et al. *Solid State Ionics* 172.1 (2004): 557-559.

5. Sugawara, Fuyuhiko, et al., *Journal of the Physical Society of Japan* 25.6 (1968): 1553-1558.

6. Reid, A. F., T. M. Sabine, and D. A. Wheeler. *Journal of Solid State Chemistry* 4.3 (1972): 400-409.

7. Yogi, Arvind, and Dinesh Varshney. *Journal of Advanced Ceramics* 2.4 (2013): 360-369.

8. Sawamoto, H. *Materials Research Bulletin* 8.7 (1973): 767-775.

9. Chamberland, B. L., and W. H. Cloud. *Journal of Applied Physics* 40.1 (1969): 434-435.

10. Rietveld, M., H.; Acta Crystallographica. 1967, 22, 15.

11. Rietveld, M., H.; Journal of Applied Crystallography.1969, 2, 65.

12. Xiao-Gang Wang, Anne Chaka, and Matthias Scheffler, *Phys. Rev. Lett.* 84, 3650 (2000)

13. Shannon, RD, *Acta crystallographica section A: crystal physics, diffraction, theoretical and general crystallography* 32.5 (1976): 751-767.

14. Shannon, RD T., and C. Tfc Prewitt. *Acta Crystallographica Section B: Structural Crystallography and Crystal Chemistry* 25.5 (1969): 925-946.

Chapter 5

On the elusive Co_2O_3 phase

Summary

Co_2O_3 is not known to occur in pure form. However, Co_2O_3 occurs as solid solutions in heavy rare earth sesquioxides such as Y_2O_3. The solid solutions are prepared by heating citrate solution at 600^{o}C. They crystallize in the cubic (c-type) bixbyite structure with the *I a-3* space group. High temperature ~ 900^{o}C annealing transforms it to the orthorhombic (*Pbnm*) distorted perovskite. XPS analysis confirms the oxidation state of Co to be +3. Magnetic measurements of cubic solid solutions indicate Co^{3+} to be in the intermediate spin state ($t_{2g}^5 e_g^1$). A comparative magnetic study on these solid solutions revealed that application of external pressure results in increase of effective magnetic moment of $Y_2O_3 \cdot Co_2O_3$ more significant than that in $Lu_2O_3 \cdot Co_2O_3$.

5.1. Introduction

It is well known that transition metal oxides are a class of compounds which shows not only diversity in the crystal structures but also elusive electronic and magnetic properties. Among all transition metal oxides, cobalt oxides are found to be exceptional and interesting because of their existence in different spin states i.e. low spin (LS), high spin (HS) and intermediate spin (IS). Besides, cobalt exhibits different oxidation states like Co^{2+} which in octahedral geometry, exists in high spin state ($t_{2g}^5 e_g^2$, $S = 3/2$) according to Hund's rule

whereas in Co^{4+}, exists in low spin state ($t_{2g}^5 e_g^0,\ S = 1/2$) in accordance with crystal field theory. Unlike these two, Co^{3+} exists in high spin state ($t_{2g}^4 e_g^2,\ S = 2$), low spin sate ($t_{2g}^6 e_g^0,\ S = 0$) and intermediate spin state ($t_{2g}^5 e_g^1,\ S = 1$). Existence of such intermediate spin states in cobalt is based on the value of crystal field splitting energy which is of same order as that of pairing energy. Also, spin state is decided by Co-O bond length and O-Co-O bond angle which is tuned by ligand effect of O on Co [1]. On the other hand, based on structural aspect it has been found that most of the 3d transition metals in +3 oxidation states form sesquioxide crystallizing in corundum type structure except Ni, Mn whereas Co_2O_3 is synthesized under high pressure, stabilized in corundum type structure and found to be exhibiting low spin to high spin state transition upon annealing [2].

Present work introduces existence of elusive Co_2O_3 in intermediate spin state in the form of solid solutions with two different rare-earth oxides synthesized under ambient pressure and high temperature.

5.2. Experimental Section

5.2.1. Synthesis

$Y_2O_3{\cdot}Co_2O_3$ [3] and $Lu_2O_3{\cdot}Co_2O_3$ solid solutions are prepared by citrate sol gel auto-combustion method. During the synthesis, 5mmoles of rare earth nitrates and 5mmoles of cobalt nitrate are dissolved in 30 ml of deionized water. About 50mmoles of anhydrous citric acid is added to the above solution and heated at 80^{o}C on heating mantle with constant stirring until it forms gel. This gel is kept inside oven at 200^{o}C for 16hrs which gives rise to porous powder which is later heated at 600^{o}C for 12hrs in presence of oxygen to remove carbonaceous content.

5.2.2. Characterization

The phase purity is confirmed by carrying out X-Ray diffraction in Bruker D8 Advance diffractometer where the sample is subjected to Cu Kα radiation in the range of Bragg angle ($10^o \leq 2\theta \leq 120^o$) under θ -2 θ scan. XRD data has been analyzed and refined using Full-Prof suite software by Rietveld refinement. X-ray photoelectron spectroscopy (XPS) carried out to determine the chemical nature of the samples using a Omicron nanotechnology spectrometer, with a monochromatic Mg K_α radiation as X-ray source with energy E = 1253.6 eV. High pressure synthesis is done in wedge shaped cubic anvil apparatus. Magnetic measurements are done in SQUID VSM (Quantum Design, USA). Temperature dependent FC (Field Cooled) and ZFC (Zero Field Cooled) magnetization data is collected at 100 Oe in the temperature range of 2 K to 390 K in vibrating sample mode.

5.3. Results and Discussions

5.3.1. Crystal Structure Analysis

The powder X-ray diffraction profiles of $Y_2O_3 \cdot Co_2O_3$ and $Lu_2O_3 \cdot Co_2O_3$ revealed that both solid solutions are crystallizing in cubic (c-type) bixbyite structure with I a-3 space group. The lattice parameters are refined using Rietveld refinement method [4-5] using fullprof package. The lattice parameters of $Y_2O_3 \cdot Co_2O_3$ found to be, a = b = c = 10.614(6) Å and for $Lu_2O_3 \cdot Co_2O_3$, a = b = c = 10.388(5) Å. Rietveld refined XRD patterns of $Y_2O_3 \cdot Co_2O_3$ and $Lu_2O_3 \cdot Co_2O_3$ are shown in the fig.5.1. (a) and (b) respectively. The refined lattice parameters, atomic co-ordinates and isotropic thermal parameters of $Y_2O_3 \cdot Co_2O_3$ and $Lu_2O_3 \cdot Co_2O_3$ are given in the Table 5.1 and 5.3 respectively and details on bond lengths are given in the Table 5.2 and 5.4 respectively.

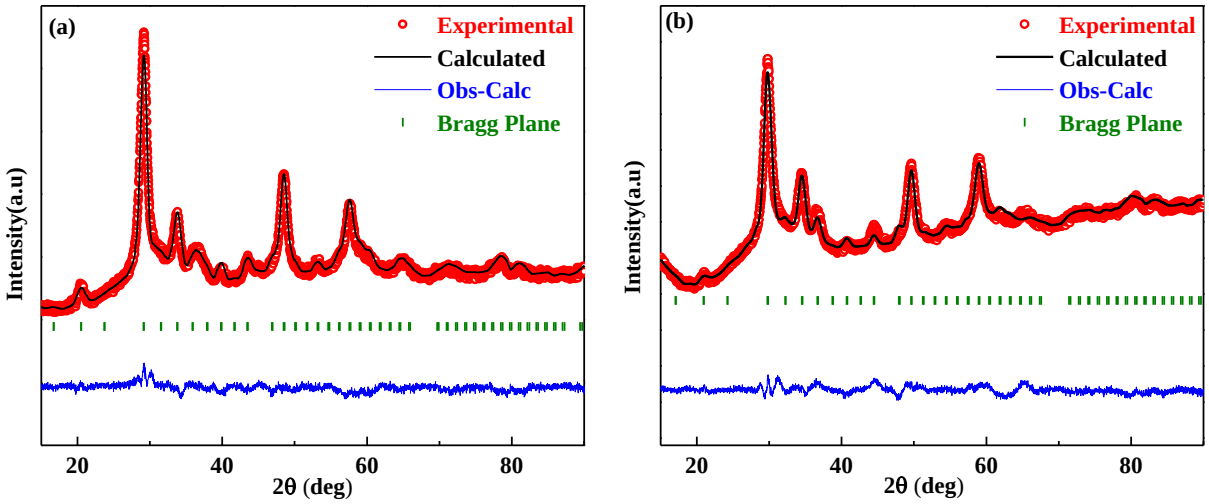

Fig.5.1. Rietveld refined X-ray diffraction pattern of (a) $Y_2O_3{\cdot}Co_2O_3$ and (b) $Lu_2O_3{\cdot}Co_2O_3$

Table 5.1: Atomic coordinates of $Y_2O_3{\cdot}Co_2O_3$

Space group : I a -3 (Cubic), a = b = c =10.614(6) Å $\alpha = \beta = \gamma = 90^o$					
Atoms	***x/a***	***y/b***	***z/c***	**B_{iso}**	**Occ.**
Y	0.25	0.25	0.25	0.58(6)	0.11(9)
Co	-0.0260(2)	0.0	0.25	0.66(9)	0.54(5)
O	0.4084(6)	0.1517(5)	0.4014(6)	1.0	1.0
$\chi^2 = 3.93\%$					

Table 5.2: Bond lengths of $Y_2O_3{\cdot}Co_2O_3$

Site	**Bond**	**Bond length (Å)**
Y	$Y - O_{(1)}$	2.550(16)
	$Y - O_{(2)}$	2.550(17)

Co	$Co–O_{(1)}$	2.389(17)
	$Co–O_{(2)}$	2.380(17)
	$Co–O_{(3)}$	1.943(17)
O	$O–O_{(1)}$	2.73(3)
	$O–O_{(2)}$	2.73(2)
	$O–O_{(3)}$	2.85(2)

Subscripts (1) to (3) used to indicate equivalent oxygen and cations in the polyhedra.

Table 5.3: Atomic coordinates of $Lu_2O_3 \cdot Co_2O_3$

Space group : I a -3 (Cubic), a = b = c =10.388(5) Å $\alpha = \beta = \gamma = 90^o$					
Atoms	***x/a***	***y/b***	***z/c***	**B_{iso}**	**Occ.**
Y	0.25	0.25	0.25	0.620	0.06(3)
Co	-0.0252(6)	0.0	0.25	0.520	0.57(0)
O	0.4185(7)	0.1653(0)	0.3349(2)	1.0	1.0
$\chi^2 = 3.9\%$					

Table 5.4: Bond lengths of $Lu_2O_3 \cdot Co_2O_3$

Site	**Bond**	**Bond length (Å)**
Lu	$Lu – O_{(1)}$	2.149(13)
	$Lu – O_{(2)}$	2.149(15)
	$Lu – O_{(3)}$	2.149(14)
	$Co–O_{(1)}$	2.851(1)

Co	Co– $O_{(2)}$	2.017(1)
	Co– $O_{(3)}$	2.324(1)
O	O – $O_{(1)}$	2.44(2)
	O – $O_{(2)}$	2.774(1)
	O – $O_{(3)}$	2.77(2)

Subscripts (1) to (3) used to indicate equivalent oxygen and cations in the polyhedra.

From the above tables it is clear that the lattice parameters of $Lu_2O_3{\cdot}Co_2O_3$is smaller than that of $Y_2O_3{\cdot}Co_2O_3$. Also, Lu-O bond length is smaller than that of Y-O. This is due to lanthanide contraction in Lu which results in decrease of ionic radii [6]. Hence Volume of $Lu_2O_3{\cdot}Co_2O_3$ is 1121.29(8) $Å^3$ which is found to be smaller than that of $Y_2O_3{\cdot}Co_2O_3$, 1196.07(9) $Å^3$.

The crystal structures of both the solid solutions are visualized using Diamond-crystal and molecular structure visualization software and shown in the Fig.5 .2.

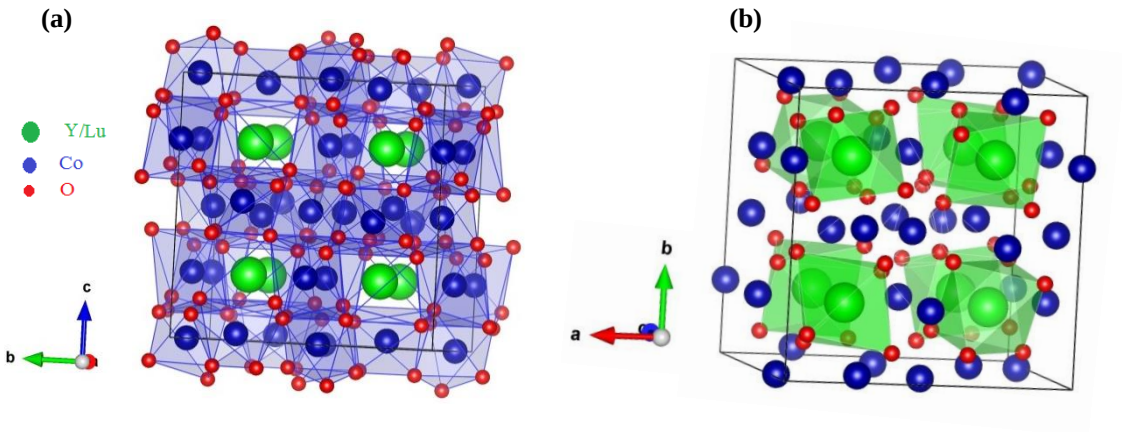

Fig.5.2. Crystal structure of $Y_2O_3{\cdot}Co_2O_3$/ $Lu_2O_3{\cdot}Co_2O_3$ (a) octahedral of Co and (b) Octahedra of Y/Lu are highlighted.

The crystal structure consists of two octahedral cation sites where Y or Lu occupies *8b* Wyckoff site and Co occupies *24d* Wyckoff sites. Only one quarter of the entire cation sites is occupied by the Y or Lu and remaining three quarters are occupied by Co ions. There are total 16

formula units in the crystal structure which is in agreement with compounds with same structure [7].

Upon annealing $Y_2O_3 \cdot Co_2O_3$ solid solution at 900°C, the phase changed to orthorhombic (Pbnm) and attained perovskite structure. The phase purity is confirmed by XRD which is shown in the Fig. 5.3(left panel) and the lattice parameters and other structural parameters are listed in the Table 5.5. Also, the bond length details are given in the Table 5.6. The crystal structure is shown in the Fig. 5.3(right panel).

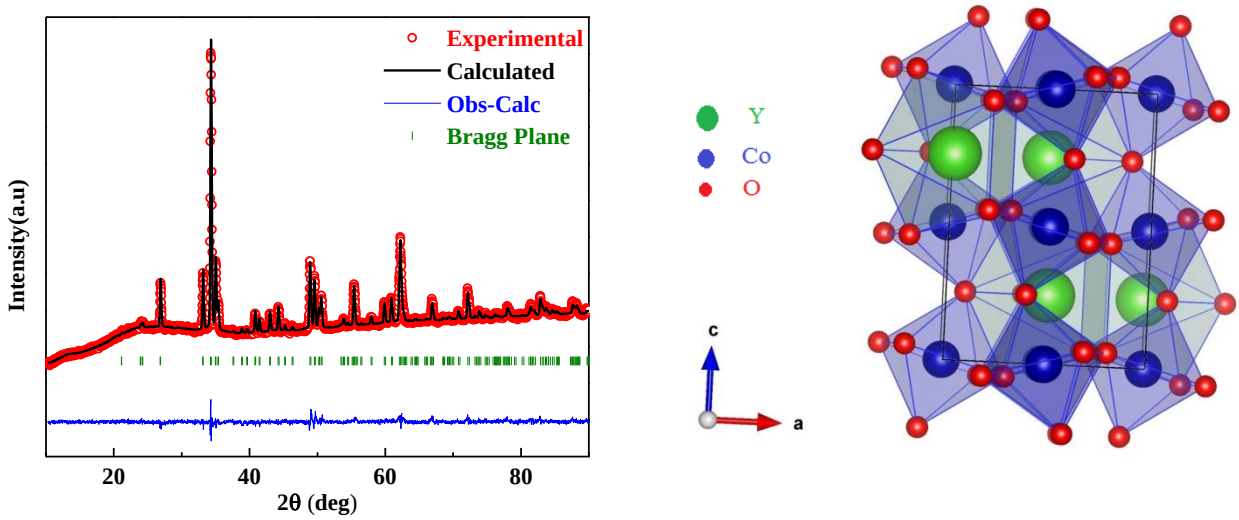

Fig.5.3. X-ray diffraction profile (left panel) and crystal structure (right panel) of $YCoO_3$

The crystal structure consists of distorted CoO_6 octahedra where Co is situated at the centre surrounded by six oxygen ions. Oxygen occupies two different sites in the crystal structure. Y resides in the voids created by the eight corner sharing octahedra[8].

Table 5.5: Atomic coordinates of $YCoO_3$

Space group : *Pbnm* (Orthorhombic), a = 5.128(3) Å, b = 5.409(2) Å, c =7.352(1) Å $\alpha = \beta = \gamma = 90^o$					
Atoms	***x/a***	***y/b***	***z/c***	**B_{iso}**	**Occ.**
Y	-0.0115(3)	-0.0678(5)	0.25	0.157(5)	0.78(4)
Co	0.5	0.0	0.0	0.028(3)	0.80(1)
O1	0.1032(3)	0.5232(4)	0.25	1.0	1.0
O2	-0.1908	0.2016(9)	0.0518(5)	1.0	1.0
$\chi^2 = 2.53\%$					

Table 5.6: Bond lengths of $YCoO_3$

Site	**Bond**	**Bond length (Å)**
Y	Y – Co	2.974(1)
	$Y – O1_{(1)}$	2.297(7)
	$Y – O1_{(2)}$	2.263(8)
	$Y – O2_{(1)}$	2.278(6)
	$Y – O2_{(2)}$	2.504(6)
	$Y – O2_{(3)}$	2.578(6)
Co	$Co– O1_{(1)}$	1.925(2)
	$Co– O2_{(1)}$	2.033(6)
	$Co– O2_{(2)}$	1.953(6)

O1	$O1 – O1_{(1)}$	3.136(9)
	$O1– O2_{(1)}$	2.771(8)
	$O1 – O2_{(2)}$	2.765(7)
	$O1 – O2_{(3)}$	2.834(8)
	$O1 – O2_{(4)}$	2.713(7)
O2	$O2 – O2_{(1)}$	2.858(8)
	$O2 – O2_{(2)}$	3.099(8)
	$O2 – O2_{(3)}$	2.779(8)
	$O2 – O2_{(4)}$	2.914(8)

Subscripts (1) to (3) used to indicate equivalent oxygen and cations in the polyhedra.

5.3.2. XPS Study

The oxidation states of Co and Y in $Y_2O_3 \cdot Co_2O_3$ and perovskite $YCoO_3$ is confirmed by XPS studies on the samples. De convoluted core level spectra of $Y_2O_3 \cdot Co_2O_3$ and $YCoO_3$ are shown in the Fig. 5.4 and 5.5 respectively. The peaks observed at 780.3eV, 786.5eV, 803.5eV and 796.2 eV in Fig 5.4(a) correspond to energy levels Co $2p_{3/2}$, Co $2p_{3/2}$ satellite, Co $2p_{1/2}$ and Co $2p_{1/2}$ satellite respectively are indicating the presence of +3 oxidation state of cobalt in $Y_2O_3 \cdot Co_2O_3$[9-10]. The peaks observed at 156.1eV and 158.1eV in Fig 5.4(b) correspond to energy levels Y $3d_{5/2}$ and Y $3d_{3/2}$ respectively are indicating the presence of +3 oxidation state of yttrium in $Y_2O_3 \cdot Co_2O_3$[11-12]. Also, peaks observed at 781eV, 787eV, 803.4eV and 796.1 eV in Fig 5.5(a) correspond to energy levels Co $2p_{3/2}$, Co $2p_{3/2}$ satellite, Co $2p_{1/2}$ and Co $2p_{1/2}$ satellite respectively are indicating the presence of +3 oxidation state of cobalt in $YCoO_3$[9-10]. The peaks observed at 156 eV and 158 eV in Fig 5.5(b) correspond to energy levels Y $3d_{5/2}$ and Y $3d_{3/2}$ respectively are indicating the presence of +3 oxidation state of yttrium in $YCoO_3$[11-12].

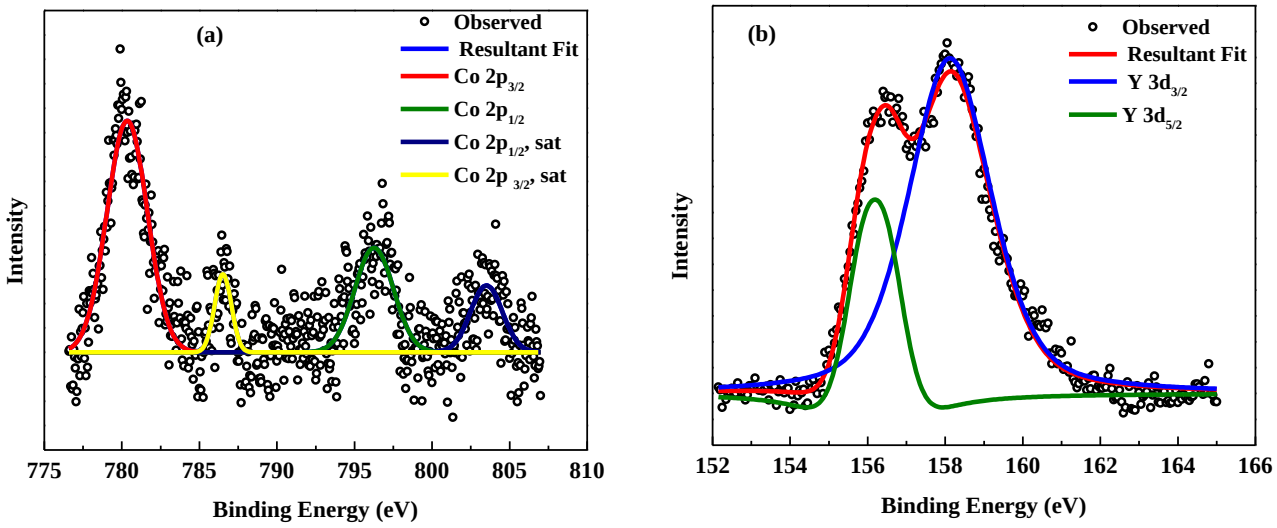

Fig.5.4. De-convoluted (a) Co 2p and (b) Y 3d core level XPS spectra of the sample $Y_2O_3 \cdot Co_2O_3$

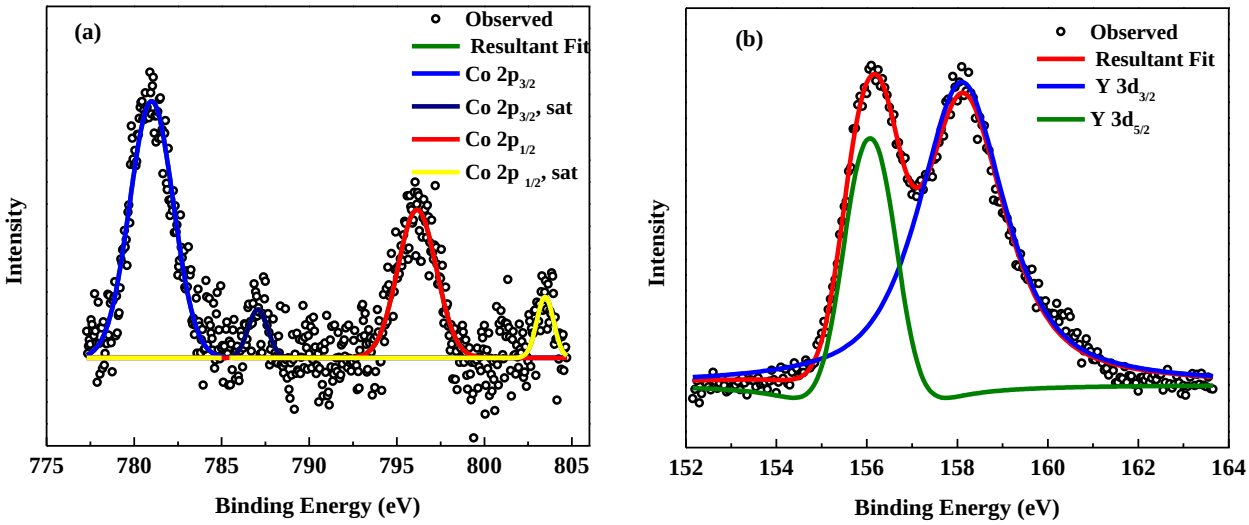

Fig.5.5. De-convoluted (a) Co 2p and (b) Y 3d core level XPS spectra of the sample $YCoO_3$

5.3.3. Magnetic measurements

Comparative study of temperature dependent field cooled (FC) magnetization under an applied DC field 100Oe of $Y_2O_3 \cdot Co_2O_3$ and $Lu_2O_3 \cdot Co_2O_3$ synthesized in ambient pressure and high pressure (100 tons) is shown in the Fig.5.6. Here, the effective magnetic moment of Co^{3+} in $Y_2O_3 \cdot Co_2O_3$ and $Lu_2O_3 \cdot Co_2O_3$ at ambient pressure calculated using Curie Weiss fit is found to be 2.1 μ_B and 2.7 μ_B respectively which is very close to the spin only magnetic moment 2.8 μ_B of Co^{3+} in intermediate spin state ($t_{2g}^5 e_g^1$). This is indicating the presence of intermediate spin state of

Co^{3+} in these solid solutions. The pictorial representation of intermediate spin state ($t_{2g}^5 e_g^1$) of Co^{3+} is shown in the Fig 5.7.

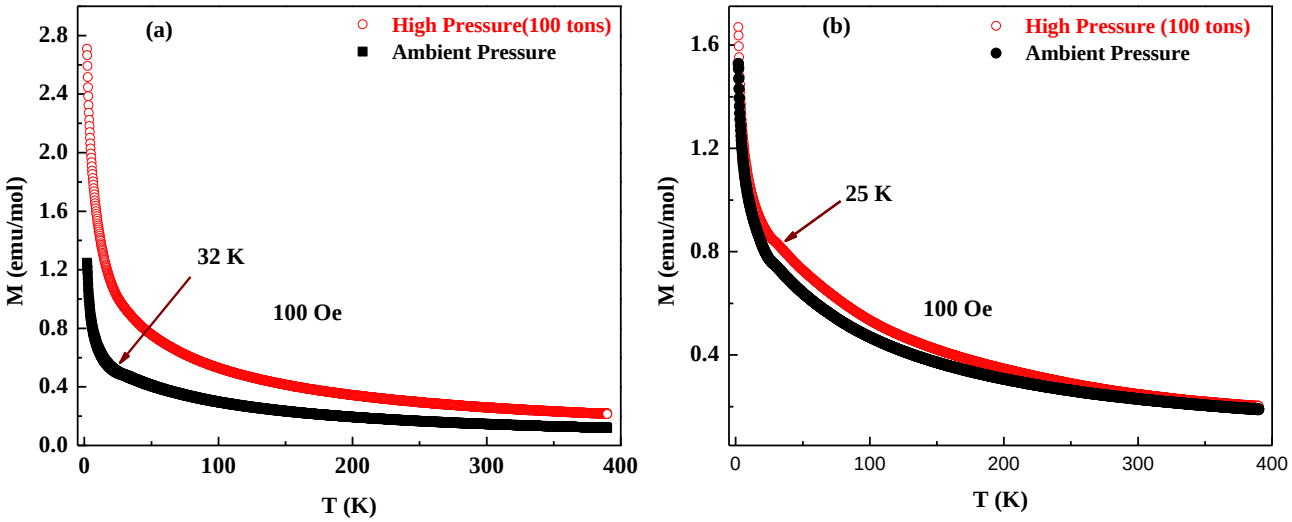

Fig.5.6. Comparative temperature dependent field cooled (FC) magnetization curves of (a) $Y_2O_3 \cdot Co_2O_3$ and (b) $Lu_2O_3 \cdot Co_2O_3$ synthesized in ambient pressure and high pressure (100 tons)

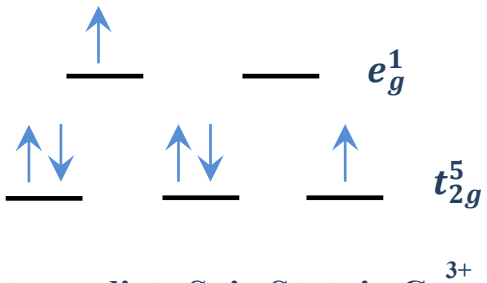

Fig.5.7. Pictorial representation of intermediate spin state of Co^{3+}

Table 5.7: μ_{eff} and θ_{CW} values for $Y_2O_3 \cdot Co_2O_3$ and $Lu_2O_3 \cdot Co_2O_3$

	$Y_2O_3 \cdot Co_2O_3$		$Lu_2O_3 \cdot Co_2O_3$	
	μ_{eff}	θ_{CW}	μ_{eff}	θ_{CW}
Ambient Pressure	2.1 μ_B	-91 K	2.7 μ_B	-90 K
High Pressure (100 tons)	2.9 μ_B	-93 K	2.8 μ_B	-82 K

Magnetic anomaly observed at T_N ~ 32 K and 25 K in FC curve of $Y_2O_3 \cdot Co_2O_3$ and $Lu_2O_3 \cdot Co_2O_3$ respectively indicating presence of long range antiferromagnetic ordering below that temperature. This is confirmed by determining θ_{CW} values using Curie Weiss law. Also, effective magnetic moment μ_{eff} is calculated using Curie Weiss fit in the paramagnetic region of inverse magnetic susceptibility curve. θ_{CW} and μ_{eff} values for $Y_2O_3 \cdot Co_2O_3$ and $Lu_2O_3 \cdot Co_2O_3$ for ambient pressure and high pressure samples are listed in the Table 5.7.

From the Table 5.2 and 5.4., it can be observed that the bond length of Co-O bond is small in case of $Y_2O_3 \cdot Co_2O_3$ than $Lu_2O_3 \cdot Co_2O_3$ which results in increased superexchange interaction in $Y_2O_3 \cdot Co_2O_3$ than $Y_2O_3 \cdot Co_2O_3$. Hence exchange energy for $Y_2O_3 \cdot Co_2O_3$ is more than $Lu_2O_3 \cdot Co_2O_3$ which helps in overcoming the thermal fluctuations and attaining magnetic ordering at high temperature. So, the Neel temperature is high in case of $Y_2O_3 \cdot Co_2O_3$ than $Lu_2O_3 \cdot Co_2O_3$. Also, $Lu_2O_3 \cdot Co_2O_3$ has greater internal pressure than in $Y_2O_3 \cdot Co_2O_3$ because of which change in μ_{eff} values are smaller in $Lu_2O_3 \cdot Co_2O_3$ than in $Y_2O_3 \cdot Co_2O_3$.

5.4. Conclusions

X-ray diffraction studies confirmed the cubic bixbyite phase of solid solutions $Y_2O_3 \cdot Co_2O_3$ and $Lu_2O_3 \cdot Co_2O_3$. Annealing $Y_2O_3 \cdot Co_2O_3$ at 900^o C converts it into orthorhombic distorted perovskite $YCoO_3$. The magnetic studies on these solid solutions revealed the presence of intermediate spin state ($t_{2g}^5 e_g^1$) of Co^{3+} in these solid solutions. Also, the presence of antiferromagnetic ordering below T_N~ 32 K and 25 K in $Y_2O_3 \cdot Co_2O_3$ and $Lu_2O_3 \cdot Co_2O_3$ respectively is observed. Application of external pressure ~ 100 tons increases the effective magnetic moment of $Y_2O_3 \cdot Co_2O_3$ effectively than that of $Lu_2O_3 \cdot Co_2O_3$.

5.5. Future Outlook

For the completion of present work, high temperature phases of $Lu_2O_3 \cdot Co_2O_3$ solid solution should be studied and the oxidation states of Co in $Lu_2O_3 \cdot Co_2O_3$ solid solution and in high temperature phase should be determined using XPS analysis. Also, the particle size determination through TEM analysis need to be done which serves as the evidence for the broadening of XRD profile peaks of $Y_2O_3 \cdot Co_2O_3$ and $Lu_2O_3 \cdot Co_2O_3$.

5.6. Bibliography

1. Raveau, Bernard, and Motin Seikh. *Cobalt oxides: from crystal chemistry to physics*. John Wiley & Sons (2012).

2. Chenavas, J., J. C. Joubert, and M. Marezio, *Solid State Communications* 9.13: 1057-1060(1971).

3. Naidu, B. S., et al. *Chemical Physics Letters* 591: 277-281 (2014).

4. Rietveld, M., H.; *Acta Crystallographica. 1967,* **22,** 15.

5. Rietveld, M., H.; *Journal of Applied Crystallography.1969,* **2,** 65.

6. Sonke, Jeroen E., and Vincent JM Salters. *Geochimica et Cosmochimica Acta* 70.6 (2006): 1495-1506.

7. Pauling, Linus, and M. D. Shappell, *Zeitschrift für Kristallographie-Crystalline Materials* 75.1 (1930): 128-142.

8. Mehta, Apurva, R. Berliner, and Robert W. Smith, *Journal of Solid State Chemistry* 130.2 (1997): 192-198.

9. Tan, Beng Jit, Kenneth J. Klabunde, and Peter MA Sherwood, *Journal of the American Chemical Society* 113.3 (1991): 855-861.

10. McIntyre, N. S., and M. G. Cook, *Analytical chemistry* 47.13 (1975): 2208-13.

11. Majumdar, Debasis, and Dilip Chatterjee, *Journal of applied physics* 70.2 (1991): 988-992.

12. Wagner C.D., Riggs W.M., Davis L.E., Moulder J.F., Muilenberg G.E.: Handbook of X-Ray Photoelectron Spectroscopy, Perkin-Elmer Corporation, Physical Electronics Division, Eden Prairie, Minn. 55344 (1979)